minerals

MDPI

Article

Platinum Group Minerals Associated with Nickel-Bearing Sulfides from the Jatobá Iron Oxide-Copper-Gold Deposit, Carajás Domain, Brazil

Yuri Tatiana Campo Rodriguez [1,2,*], Nigel J. Cook [1], Cristiana L. Ciobanu [1], Maria Emilia Schutesky [2], Samuel A. King [1], Sarah Gilbert [3] and Kathy Ehrig [1,4]

[1] School of Chemical Engineering, The University of Adelaide, Adelaide, SA 5005, Australia; nigel.cook@adelaide.edu.au (N.J.C.); cristiana.ciobanu@adelaide.edu.au (C.L.C.); samuel.king@adelaide.edu.au (S.A.K.); kathy.ehrig@bhp.com (K.E.)
[2] Geosciences Institute, University of Brasília, Brasília 70910-900, DF, Brazil; maria_emilia@unb.br
[3] Adelaide Microscopy, The University of Adelaide, Adelaide, SA 5005, Australia; sarah.gilbert@adelaide.edu.au
[4] BHP Olympic Dam, 10 Franklin Street, Adelaide, SA 5000, Australia
* Correspondence: yuri.camporodriguez@adelaide.edu.au

Abstract: An enrichment in nickel (Ni) or platinum group elements (PGE) is seldom observed in ores of the iron oxide–copper–gold (IOCG) type. This phenomenon is, however, known from a few deposits and prospects in the Carajás Mineral Province, Brazil. The Ni-PGE enrichment is explained, in part, by the spatial association of the IOCG-type ores with altered mafic-ultramafic lithologies, as well as by reworking and remobilization of pre-existing Ni and PGE during multiple mineralization and tectonothermal events across the Archean-Proterozoic. One such example of this mineralization is the Jatobá deposit in the southern copper belt of the Carajás Domain. This is the first detailed study of the Ni and PGE mineralization at Jatobá, with implications for understanding ore genesis. Petrographic and compositional study of sulfides shows that pyrite is the main Ni carrier, followed by pyrrhotite and exsolved pentlandite. Measurable concentrations of palladium (Pd) and platinum (Pt), albeit never more than a few ppm, are noted in pyrite. More importantly, however, the trace mineral signature of the Jatobá deposit features several platinum group minerals (PGM), including merenskyite, naldrettite, sudburyite, kotulskite, sperrylite, and borovskite. These PGM occur as sub-10 µm-sized grains that are largely restricted to fractures and grain boundaries in pyrite. All Pd minerals reported contain mobile elements such as Te, Bi, and Sb and are associated with rare earth- and U-minerals. This conspicuous mineralogy, differences in sulfide chemistry between the magnetite-hosted ore and stringer mineralization without magnetite, and microstructural control point to a genetic model for the sulfide mineralization at Jatobá and its relative enrichment in Ni and PGE. Observations support two alternative scenarios for ore genesis. In the first, an initial precipitation of disseminated or semi-massive Ni-PGE-bearing sulfides took place within the mafic rock pile, possibly in a VHMS-like setting. Later partial dissolution and remobilization of this pre-existing mineralization by mineralizing fluids of IOCG-type, possibly during the retrograde stage of a syn-deformational metamorphic event, led to their re-concentration within magnetite along structural conduits. The superposition of IOCG-style mineralization onto a pre-existing assemblage resulted in the observed replacement and overprinting in which PGE combined with components of the IOCG fluids like Sb, Bi, and Te. An alternative model involves leaching, by the IOCG-type fluids, of Ni and PGE from komatiites within the sequence or from ultramafic rocks in the basement. The discovery of PGM in Jatobá emphasizes the potential for additional discoveries of Ni-PGE-enriched ores elsewhere in the Carajás Domain and in analogous settings elsewhere.

Keywords: Carajás Mineral Province; Jatobá; IOCG systems; sulfide minerals; nickel; platinum group minerals

Citation: Campo Rodriguez, Y.T.; Cook, N.J.; Ciobanu, C.L.; Schutesky, M.E.; King, S.A.; Gilbert, S.; Ehrig, K. Platinum Group Minerals Associated with Nickel-Bearing Sulfides from the Jatobá Iron Oxide-Copper-Gold Deposit, Carajás Domain, Brazil. *Minerals* **2024**, *14*, 757. https://doi.org/10.3390/min14080757

Academic Editor: Olivier Blein

Received: 26 June 2024
Revised: 22 July 2024
Accepted: 23 July 2024
Published: 26 July 2024

1. Introduction

Iron oxide-copper-gold (IOCG) deposits encompass a variety of mineralization styles and geological settings unified by a dominance of iron oxides (e.g., [1,2]). Research in the 30 or so years since the term 'IOCG deposit' was first used [3] has significantly advanced understanding of their origin, even if some aspects of their genesis remain ill constrained, while others continue to be controversial. Although implicitly concentrating copper and gold, along with subordinate silver, and in rare cases, also uranium, some IOCG systems have attracted attention in recent years due to the recognized relative enrichment of valuable critical elements such as Co and rare earth elements (REE) [2]. In contrast, IOCG deposits are not generally noted for an enrichment in nickel (Ni) or platinum group elements (PGE), yet recent discoveries have led to IOCGs, among other deposit types, to be touted as potential future sources of Ni and other valuable metals, e.g., [4].

The Neoarchean Carajás Mineral Province (CMP; Figure 1) is located in the southeastern portion of the Amazonian Craton, Brazil. In addition to several other genetic types of mineralization, IOCGs are a prominent style of mineralization within the Carajás Domain. These deposits occur within varied host lithologies that have geological ages spanning the Neoarchean and Paleoproterozoic [5–10]. The Carajás Domain of the CMP is one of the world's largest IOCG provinces [11]. Giant copper reserves occur in deposits such as including, Sossego-Sequeirinho [12–14], Salobo [15–17], Igarapé Bahia [18,19], and many others.

Although a relative enrichment of Ni in the IOCG deposits is atypical and not fully understood, some Carajás ore systems represent attractive exploration targets due to the presence of this high-value metal. Among the deposits classified as IOCGs that display an enrichment of Ni is Jatobá, a medium-sized deposit within an IOCG orefield that includes Sossego-Sequeirinho. Lithologies present in the Jatobá deposit include a series of mafic-ultramafic sequences, metabasaltic units, altered volcanoclastic breccias, and minor felsic volcanic units. The Jatobá deposit lies immediately north of a major fault and thrust zone between Mesoarchean mafic and ultramafic rocks and the Grão Para Group of the Itacaiúnas Supergroup, comprising Neoarchean bimodal volcanic sequences. Jatobá displays a spatial association yet arguably ambiguous genetic relationship with altered mafic-ultramafic lithologies [20].

Other Ni-enriched systems in the Carajás Domain are affiliated to the IOCG class, or to what is proposed as a "continuum between IOCGs and hydrothermal Ni deposits", the latter being a rather rare, enigmatic, and only recently identified class of unconventional ores [21]. Nickel-enriched systems in the Carajás Domain include the Ni-dominant Jaguar deposit [22–24], the GT-34 prospect [25], Cristalino [26], and Castanha [27]. In the cited publications, the anomalous enrichment in Ni has typically been explained, admittedly in often rather vague terms, by invoking the contribution of deep, high-temperature fluids of (ortho)magmatic origin or an affinity to the deeper zones of an IOCG system. The relative abundance of Ni-laterites associated with Neoarchean mafic-ultramafic complexes clearly indicates that Ni is widespread within supracrustal rocks of the Carajás Domain. We also note the report of spinifex-textured komatiites in the Selva greenstone belt, close to Jatobá [28]. This wealth of nickel in the Carajás Domain opens up not only the possibility of early mineralization stages within IOCG genesis but also the leaching, remobilization, and recycling of Ni, PGE, and to some extent, also Co and Cr, from pre-existing mineralization during a later IOCG-type event. The potential for new discoveries in the region has catalyzed new work aiming at identifying structural controls and relationships between the deposits and deep architecture, e.g., [29].

Although the nickel endowment of the Jatobá deposit has been noted previously [20], the present contribution sets out to establish a detailed understanding of ore mineralogy and how it has evolved over geological time. We focus on both the major and minor ore components of the ores, as well as on trace elements hosted by common sulfides. Importantly, this contribution describes the presence of Pd and Pt within common sulfides and as discrete platinum group minerals (PGM). The distinct geochemical-mineralogical signature of the sulfide assemblages from Jatobá is evaluated in the context of geological

setting, host rocks, and geological history. This represents the first report of PGM from an IOCG system in the Carajás Domain, even though "Pd-rich melonite" is reported (without composition provided) from Sossego [12]. Mansur et al. [24] provided evidence for traces of PGE from the base metal sulfides in the Jaguar deposit. Although mostly below minimum limits of detection in most cases (~0.1 ppm), concentrations up to 1 ppm were noted in pentlandite. They also noted low but still measurable concentrations of Ru, Rh, Ir, and Os in pyrite.

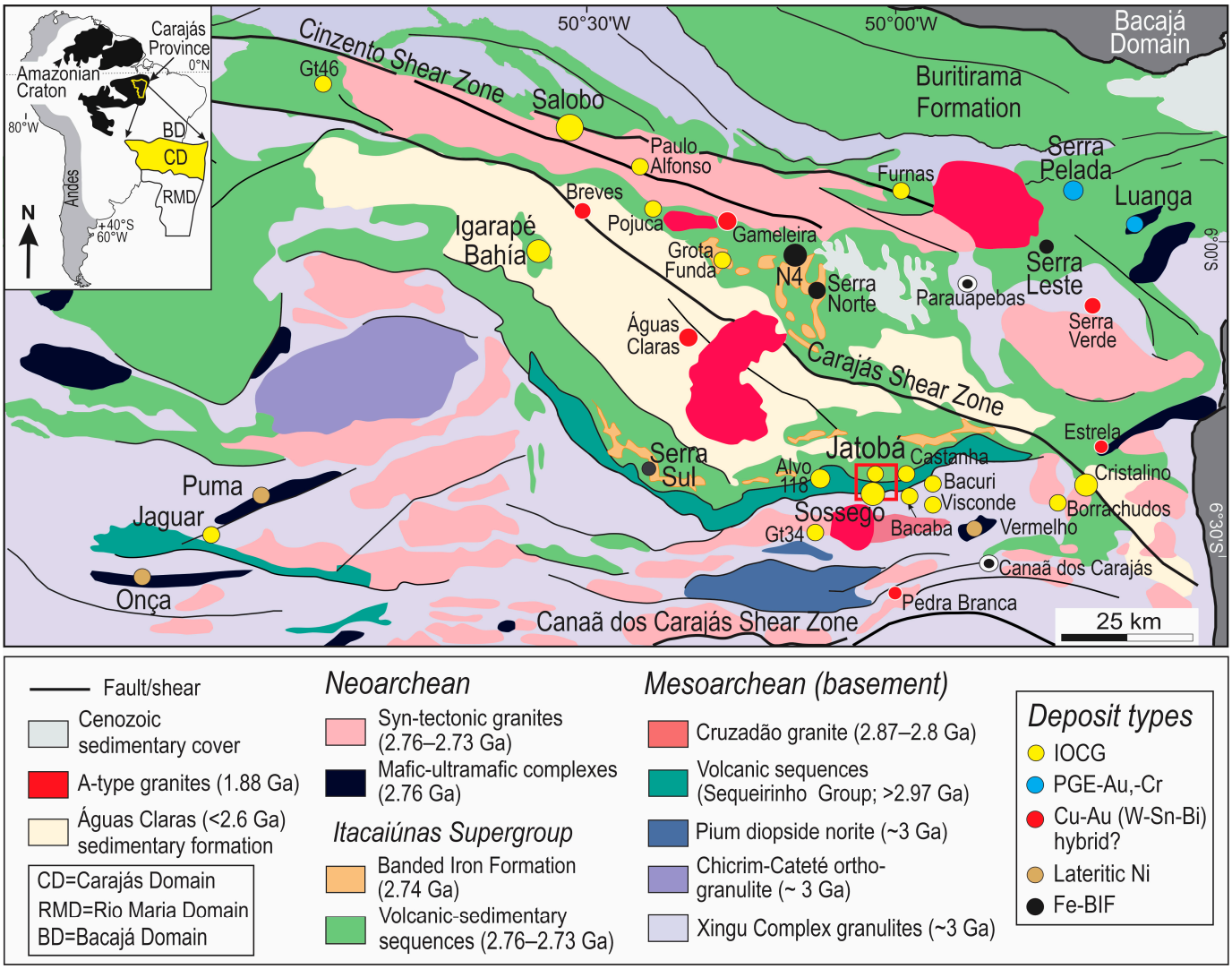

Figure 1. Geological map of the Carajás Domain showing the location of Jatobá orefield (red rectangle). Modified from Vasquez et al. [30] and Tavares et al. [7]. Named deposits referred to in the text are indicated. Deposit types are from Grainger et al. [5] and Trunfull et al. [9]. Circles indicate the relative sizes of the deposits. The inset shows the location of the Carajás Domain within the Amazonian Craton, South America.

2. Background

2.1. Geology and Geological Evolution of the Carajás Domain

The Carajás Mineral Province in the Amazonian Craton of Brazil (e.g., [30]) is one of the largest metallogenic belts on Earth. It comprises two major tectonostratigraphic domains: the Carajás Domain in the north, which hosts Neoarchean IOCG deposits and Paleoproterozoic Cu-Au mineralization, and the Rio Maria Domain (RMD) to the south with its Mesoarchean lode-Au deposits (e.g., [31]). Several other styles of mineralization

are recorded, spanning ages from 2.6 Ga to 1.6 Ga [9]. The Carajás Mineral Province is bound to the north by the Bacajá Domain (BD on the inset to Figure 1).

In brief, the Carajás Domain (equivalent to the Itacaiúnas Belt of Araújo et al. [32] is composed of a Mesoarchean basement made up of orthogranulites, gneisses and migmatites, granites, and the 3–2.9 Ga greenstone belts of the Sequeirinho Group (Figure 1; [7,33]). These oldest rocks experienced overprinting multiple times during the Archean and Paleoproterozoic. The basement is covered by Neoarchean (2.76–2.73 Ga) volcano-sedimentary sequences of the Itacaiúnas Supergroup (e.g., [31,34]). Lithologies within the Itacaiúnas Supergroup [33,35] include basaltic lithologies of the Grão Para Group, which host the Jatobá deposit.

Neoarchean igneous activity is represented by mafic-ultramafic complexes (e.g., [33]), syntectonic and A-type granites [7,36,37]. Other important igneous events include the peralkaline to meta-aluminous intrusions of Old Salobo (2573 ± 3 Ma [16,33]). Less voluminous Itacaiúnas granites (2560 ± 37 Ma; [33] are identified within the Cinzento shear zone [16]. Further anorogenic A-type granites were emplaced at 1.88–1.86 Ma during the Transamazonian orogeny (e.g., [38,39]).

Paleoproterozoic sedimentary rocks define the Águas Claras Formation and unconformably overlie the abovementioned lithostratigraphic units. These are sandstones and siltstones deposited in fluvial to shallow marine environments and outcrop mainly in the central part of the Carajás District [40].

Several publications (e.g., [7,9,31,34]) cover the geodynamic evolution of the Carajás Domain and the implications this has for metallogeny. There is little consensus about the timing of the IOCG systems in the literature or whether or not these systems are associated with magma-derived fluids (magmatic-hydrothermal IOCG type *sensu stricto*). Several recent publications consider there were at least two events in which IOCG deposits formed [9,10,31]. By far the most innovative and somewhat non-conventional geodynamic model for the Carajás Domain is that of Costa et al. [31] who attribute the deposition of the early Itacaiúnas Supergroup during the Mesoarchean (2.87–2.83 Ga), at least for some districts, such as Rio Novo. This is followed by BIF deposition (in the Salobo-Pojuca Formation) during a ~70 Ma-long (2.83–2.76 Ga) magmatic quiescence. The first IOCG event is placed during Neoarchean deformation associated with a transtensional or transpressional strike-slip regime at 2.76–2.73 Ga, after the deposition of the Itacaiúnas Supergroup. We note that this same time interval is generally attributed to the Itacaiúnas Supergroup (Figure 1). Based on the ages of crosscutting dykes and an alkaline granite in the case of Salobo, the second IOCG event, at <2.6 Ga, occurred in an extensional rifting to passive margin geotectonic setting [9].

Trunfull et al. [9] also considered two IOCG events occurring within transpressional or transtensional regimes, both being post-Itacaiúnas Supergroup deposition (rifting at 2.76 Ga). In this model, several scenarios are discussed. These involve either basin inversion (commencing at 2.74 Ga) followed by more basin inversion or rifting (2.72–2.68 Ga), which is also the interval of the first IOCG event. We note that this time interval follows the deposition of the Itacaiúnas Supergroup. A yet more recent interval (2.6–2.45 Ga) is provided for an IOCG event in the Northern Copper Belt, during episodic reactivation of the "Cinzeto Shear Zone and metamorphism". In either case, coeval volcanism or emplacement of (syn-tectonic) granitoids is inferred to occur contemporaneously with the IOCG events.

The younger 2.55 Ga age of IOCG deposits in the Northern Copper Belt is reiterated in a study of boron isotopes [41]. This study considers the formation of seafloor hydrothermal systems with hydrothermal vents during the 2.76–2.73 Ga interval prior to the leaching of older seafloor exhalative rocks by "magmatic-hydrothermal fluids to form the IOCG deposits of the Carajás Province".

2.2. IOCG Deposits of the Carajás Domain

The Carajás Domain hosts IOCG deposits (Figure 1), characterized by multiple Archean-Paleoproterozoic episodes of mineralization within two major regional structures, the Canaã dos Carajás and Cinzento shear zones [9]. A generic model for Neoarchean IOCG systems is provided by Schutesky and Oliviera [8]. This model considers the significance of crustal shear zones to drive upward fluid flow of 'magmatic-hydrothermal fluids', with this latter term used explicitly to highlight the high temperature of the fluids derived from inferred, deep-seated intrusions, as well as the magmatic isotopic signatures recorded in all IOCG deposits studied so far in the Carajás Province. IOCG mineralization is attributed to 2.76–2.73 Ga, i.e., coeval with bimodal magmatism in the Itacaiúnas Supergroup. The large compilation of geochronological data provided by Trunfull et al. [9] places IOCG genesis at 2.72–2.68 Ga, after deposition of the Itacaiúnas Supergroup at ~2.76 Ga in a rift formed during an extensional regime. Recently, the proposed temporal link between granitic magmatism and IOCG deposits in the Carajás Domain has been questioned [10]. The latter authors argue for a slightly younger age of IOCG genesis and contend that hydrothermal activity took place after granite emplacement (2.72–2.68 Ga and again at 2.59–2.53 Ga).

IOCG systems in the Carajás Domain commonly display Na-, Na-Mg/Ca alteration with scapolite-grunerite-hastingsite, followed by Ca-Fe assemblages (actinolite-magnetite-apatite) and K-Fe (biotite and K-feldspar). The late alteration stage is propylitic (chlorite-epidote), accompanied by hydrolytic (veinlet) alteration and carbonatization [8,11].

Magnetite is the dominant iron oxide, and chalcopyrite ($CuFeS_2$) is the main expression of copper enrichment ([8] and references therein). The deposits have variable enrichment in Ni, Co, Pb, and Zn [5]. Tin is also reported in the form of cassiterite from the Sequeirinho/Sossego mines [12,14]. Ore mineralogy is, however, relatively consistent across the province, irrespective of their local settings and host rocks.

A later IOCG event is proposed to have occurred at 1.88 Ga and is widely attributed to the waning stages of the Transamazonian Orogeny [42]. There is, however, uncertainty about whether this is a distinct event or simply a Cu-Au overprint or remobilization superimposed onto a pre-existing IOCG deposit.

2.3. Nickel and Platinum Group Element Endowment in the Carajás Domain

A detailed treatment of the diverse and complex metallogeny and timeframe of the Carajás Mineral Province [5,9] is beyond the scope of the present contribution. Of importance here, however, is that the northern Carajás Domain hosts many other deposits alongside the IOCG deposits [11,43], of which Sossego and Salobo are perhaps among the best known. Among the other deposit styles are the giant Serra Norte iron ores and several deposits related to mafic-ultramafic complexes of ~2.76–2.72 Ga age, including the Luanga and Lago Grande Complexes [33,44]. These mafic-ultramafic complexes constitute a major magmatic event that intrudes Mesoarchean units and is coeval with the extensive basaltic volcanism of the Grão Pará Group [33,34].

There are three main types of mineralization associated with these layered complexes. Firstly, the world-class laterite nickel–cobalt deposits such as Serra da Onça-Puma, Vermelho, and Jacaré-Jacarezinho are associated with major structures along the Southern Copper Belt, such as the Canaã dos Carajás shear zone and McCandless fault system [8,28]. Secondly, there are the sulfide-rich PGE-Cr and PGE-Au deposits such as Luanga and Lago Grande [38,45–47]. Various PGM, including kotulskite, palarstanide, sperrylite, paolovite, arsenopalladinite, and hollingworthite, are documented from Luanga and Lago Grande [44,47]. A third type of mineralization is represented by Serra Pelada, an enigmatic, exceptionally high-grade Au-Pd-Pt deposit [48], in which multiple rare PGMs have been identified [49,50]. The deposit formed at 1.88–1.86 Ga [5] and, although not fully understood, is widely assumed to have been formed by leaching and remobilization of metals from ultramafic complexes [44]. The contribution of metals from mafic-ultramafic

complexes has also been invoked to explain the relatively high Ni-Co contents noted in Cu-Au deposits [11].

A distinct group of Cu-Au deposits with different mineralization styles yet conspicuously lacking iron oxides are observed associated with a Paleoproterozoic (ca. 1.9–1.8 Ga) anorogenic an alkaline to sub-alkaline plutonic event (e.g., Serra dos Carajás, Young Salobo, Pojuca, and Cigano [14,33], and references therein). These deposits are sulfide-quartz-rich with a variable content of F, B, and Li [5,51]. Pollard et al. [51] suggested that these Paleoproterozoic Cu-Au deposits represent the expression of thermal remobilization or the reactivation of older structures and associated mineralization.

2.4. The Jatobá Deposit

Jatobá is one of a cluster of four ore deposits in the southern copper belt of the Carajás Domain (Figure 2A). Each of the four deposits (Pista, Sequeirinho, Sossego, and Jatobá) lies along the E-W-striking structures of the Canaã dos Carajás shear zone system. Fabrics in ores and host rocks are characterized by widespread mylonitic foliation attributable to this structural control. Jatobá is, however, unique in being the only one hosted by rocks of the Neoarchean Grão Para Group. Age constraints on mineralization were provided by Moreto et al. [37] for Sequeirinho (2712 Ma, U-Pb monazite) and Pista (2710–2685 Ma, Re-Os molybdenite) orebodies. Sossego provided a younger U-Pb monazite age of 1904–1879 Ma, but it is hosted within an older (2740 Ma) granite [37].

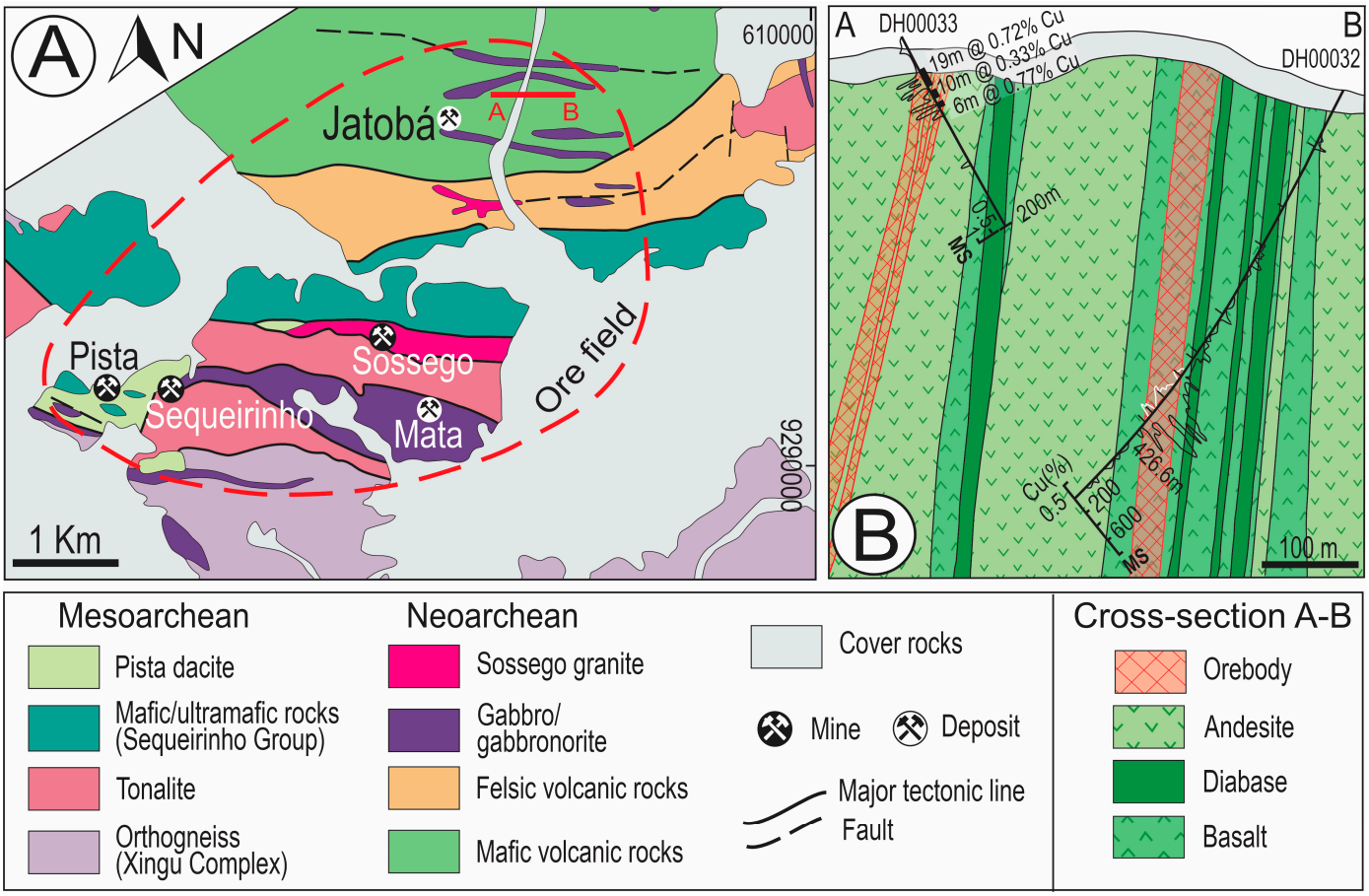

Figure 2. (**A**) Simplified geological map of the Jatobá-Pista-Sequeirinho-Sossego orefield map (modified after Veloso et al. [20]. (**B**) E-W cross-section A-B as marked on (a) indicating sampled drillhole DH00032, host lithologies Cu grades, and magnetic susceptibility (MS).

Exploration of the Jatobá deposit has been sporadic and is presently dormant. Except for Veloso et al. [20], who considered magnetite formation "at the transition from magmatic

to deep magmatic-hydrothermal systems, including the IOA deposits, especially on the onset of the early nickel-enriched mineralization stage", little information is available in the public domain. Prior publications, including Veloso et al. [20], cite the resource and grade of the Pista-Sequeirinho-Sossego orefield as 355 Mt @ 1.5% Cu and 0.28 g/t Au, drawing on data originally provided in a conference abstract by Lancaster et al. [52]. We are unaware of any published resource data for nickel or PGE in the Jatobá deposit, nor of any publicly available information on the distribution of Ni or PGE at the deposit scale, apart from the statement that Ni contents are higher in massive magnetite-sulfide ore [20]. Veloso [53] provides some "lithochemical data for ore samples" that includes 1270–3930 ppm Ni, 670–2320 ppm Co, 81–372 ppb Pd, and 2–17 ppb Pt.

A major E-W fault separates rhyolites and dacites from the main body of dominantly mafic lithologies that host Jatobá (amygdaloidal basalts and andesites but considered rhyodacites by Veloso et al. [20]. In a previous study of eight drillholes from Jatobá that intersect a 250 m-wide orezone [20,53], the deposit is said to be hosted by "Itacaiúnas rhyodacites and felsic volcaniclastic breccias in the footwall zone, and amygdaloidal basalts associated with mafic tuffs in the hanging wall". Veloso et al. [20] go on to describe a protolith defined by an assemblage of andesine + actinolite onto which eleven pre-, syn-, and late-tectonic alteration stages are superimposed. Proximal (scapolite-hastingsite) and distal (albite-scapolite-quartz-magnetite-biotite) zones are identified.

Sulfide orebodies occur as relatively narrow zones that are spatially associated with magnetite-apatite mineralization and form sub-vertical lenses located close to diabase dikes and contact zones within the mafic lithologies (Figure 2B). Copper and Ni minerals are concentrated within pyrite-pyrrhotite ores that occur as disseminations within magnetite and as veins oriented parallel to the biotite-chlorite mylonitic foliation [20]. The presence of ferrotschermakite, Mg-amphiboles, and non-classical pyriboles (NCPs) preserved as nanoscale inclusions within magnetite enabled Campo-Rodriguez et al. [54] to arrive at the realization that the magnetite had undergone metamorphism at amphibolite facies conditions, consistent with deep burial.

3. Samples and Analytical Methodology

Our set of ten representative samples from the Jatobá deposit derived from a drillhole (Figure 2B; DH0032) that intersects magnetite-rich parts of the deposit and covers dominantly mafic lithologies. Twelve polished thin sections were examined using a reflected light microscope and subsequently using an FEI Quanta 450 field emission scanning electron microscope (SEM) (FEI Company, Hillsboro, OR, USA) in backscatter electron (BSE) mode. The SEM is housed at Adelaide Microscopy, The University of Adelaide, and is equipped with a silicon-drift energy-dispersive X-ray spectrometer. Energy-dispersive X-ray spectrometry (EDS) is utilized for mineral identification. SEM examination allowed for detailed assessment of microstructural features, grain size, morphology, relationships between main minerals, and identification of fine-grained accessory phases.

LA-ICP-MS trace element spot analysis and mapping was undertaken using a RESOlution-SE 193 nm Excimer laser (Applied Spectra, Inc., West Sacramento, CA, USA) coupled to an Agilent 8900x quadrupole ICP mass spectrometer (Agilent Technologies, Inc., Santa Clara, CA, USA) in the same laboratory. Background measurement was 30 s, followed by the acquisition of a signal during ablation of 50 or 60 s. The following thirty-six isotopes were measured, with corresponding dwell times (in ms) provided in brackets: ^{27}Al (5) ^{34}S (5), ^{49}Ti (5), ^{55}Mn (10), ^{57}Fe (5), ^{59}Co (10), ^{60}Ni (10), ^{65}Cu (10), ^{66}Zn (10), ^{75}As (10), ^{77}Se (20), ^{88}Sr (10), ^{90}Zr (5), ^{95}Mo (20), ^{105}Pd (30), ^{106}Pd (30), ^{107}Ag (20), ^{111}Cd (10), ^{113}In (10), ^{115}In (10), ^{118}Sn (10), ^{121}Sb (10), ^{125}Te (20), ^{182}W (10), ^{193}Ir (30), ^{195}Pt (30), ^{197}Au (30), ^{204}Pb (10), ^{205}Tl (10), ^{206}Pb (10), ^{207}Pb (10), ^{208}Pb (10), ^{209}Bi (10), ^{232}Th (10), and ^{238}U (10). Longer dwell times were employed for isotopes of greatest interest. For all analyses, reference materials STD-GL3 [55], NiS-3 [56], and GSD-1G (USGS) were analyzed before, during, and after pyrite ablation. The laser spot diameter was a consistent 50 µm diameter at a pulse repetition rate of 5 Hz and fluence of 3 J/cm^2. Iron was used as an internal calibration

standard for pyrite and pyrrhotite, whereas Cu was used for chalcopyrite. Stoichiometric compositions were assumed in all cases.

Typical minimum detection limits (mdl, in ppm) for isotopes measured quantitatively are as follows: ^{55}Mn (0.05), ^{57}Fe (2), ^{59}Co (0.03), ^{60}Ni (0.03), ^{65}Cu (0.05), ^{66}Zn (0.12), ^{75}As (0.3), ^{77}Se (0.7), ^{95}Mo (0.03), ^{105}Pd (0.0002), ^{106}Pd (0.0002), ^{107}Ag (0.0006), ^{111}Cd (0.001), ^{113}In (0.003), ^{115}In (0.003), ^{118}Sn (0.06), ^{121}Sb (0.03), ^{125}Te (0.06), ^{182}W (<0.0001), ^{195}Pt (0.0005), ^{197}Au (0.0003), ^{204}Pb (0.006), ^{206}Pb (0.001), ^{207}Pb (0.001), ^{208}Pb (0.001), ^{209}Bi (0.003), and ^{238}U (<0.0001). No quantitative data are presented for Al, S, Ti, Mn, Cu, Zn, Sr, and Zr, as isotopes of these elements were measured only to identify the presence of inclusions. Tungsten, Ir, Tl, and Th were consistently at or below their respective mdl values in all analyses and are also not tabulated. Rhodium, Ru, and Os are not present in available reference materials and were therefore not quantified. Based on measurement of Pt, Pd and Ir, however, they are very likely to be extremely low and probably <mdl.

LADR software version 1.1.07 (Norris Scientific Pty Ltd., Kingston, Hobart, TAS, Australia) was utilized for data processing. Total Pb concentration data provided in Table 1 were calculated as the sum of ^{204}Pb, ^{206}Pb, ^{207}Pb, and ^{208}Pb. The areas selected for analysis were carefully chosen to avoid inclusions and the time-resolved depth profiles for each ablation spot were carefully examined for evidence of sub-surface inclusions or other artefacts that could bias results and interpretation. Where obvious inclusions were noted, the integrated interval was modified to avoid them. Data indicative of abundant inclusions or obvious mineral mixtures were rejected.

Table 1. Compositional data (SEM-EDS) for selected PGM.

	1	2	3	4	5
	Bi-Bearing Merenskyite (Jt4)	**Merenskyite (Jt9)**	**Ni-Bi-Bearing Merenskyite (Jt9)**	**Merenskyite (Jt8)**	**Naldrettite (Jt10)**
	Mean (n = 4, single grain)	Mean (n = 3, single grain)	Mean (n = 4, single grain)		
Pd	27.8 ± 1.53	29.9 ± 0.60	22.3 ± 0.29	26.9	67.0
Bi	16.4 ± 0.76	2.1 ± 0.2	15.8 ± 1.11		
Te	53.4 ± 2.10	67.9 ± 0.40	54.5 ± 2.50	73.1	
Pt			3.4 ± 0.10		
Ni		2.4 ± 0.07	1.8 ± 0.26		
Sb					33.0
Total	97.6 ± 3.03	100.1 ± 0.06	97.7 ± 1.67	100.0	100.0

Calculated formulae: 1. $Pd_{1.03}(Te_{1.66}Bi_{0.31})_{1.97}$, 2. $(Pd_{1.00}Ni_{0.09})_{1.09}(Te_{1.89}Bi_{0.02})_{1.91}$, 3. $(Pd_{0.83}Ni_{0.12}Pt_{0.07})_{1.02}(Te_{1.69}Bi_{0.30})_{1.98}$, 4. $Pd_{0.92}Te_{2.08}$, 5. $Pd_{2.10}Sb_{0.90}$.

For element imaging, the laser was rastered across the sample, forming a rectangular grid across the area of interest with a beam size of 10 µm. Rasters were then compiled and processed into trace element intensity maps using 'Iolite' software [57], version Iolite 3, with extension Igor Pro 6.37 used for the generation of laser maps. Mapped intensities are scaled independently for each element to enhance different features; unless stated otherwise, the scale used is logarithmic (10^n). Similar values between ^{105}Pd and ^{106}Pd were checked to avoid any interference from inclusions of chalcopyrite for ^{105}Pd and sphalerite for ^{106}Pd. ^{57}Fe was selected as the internal standard, assuming ideal stoichiometry for the sulfides.

4. Results

The studied samples cover a ~450 m-long interval and represent different assemblages within mafic lithologies (Figure 3A). The orebody intersected by this drillcore is a magnetite-rich interval, ca. 50 m in length, with grades of ~0.5% Cu situated in the lower part of the drillhole (samples Jt7–Jt10).

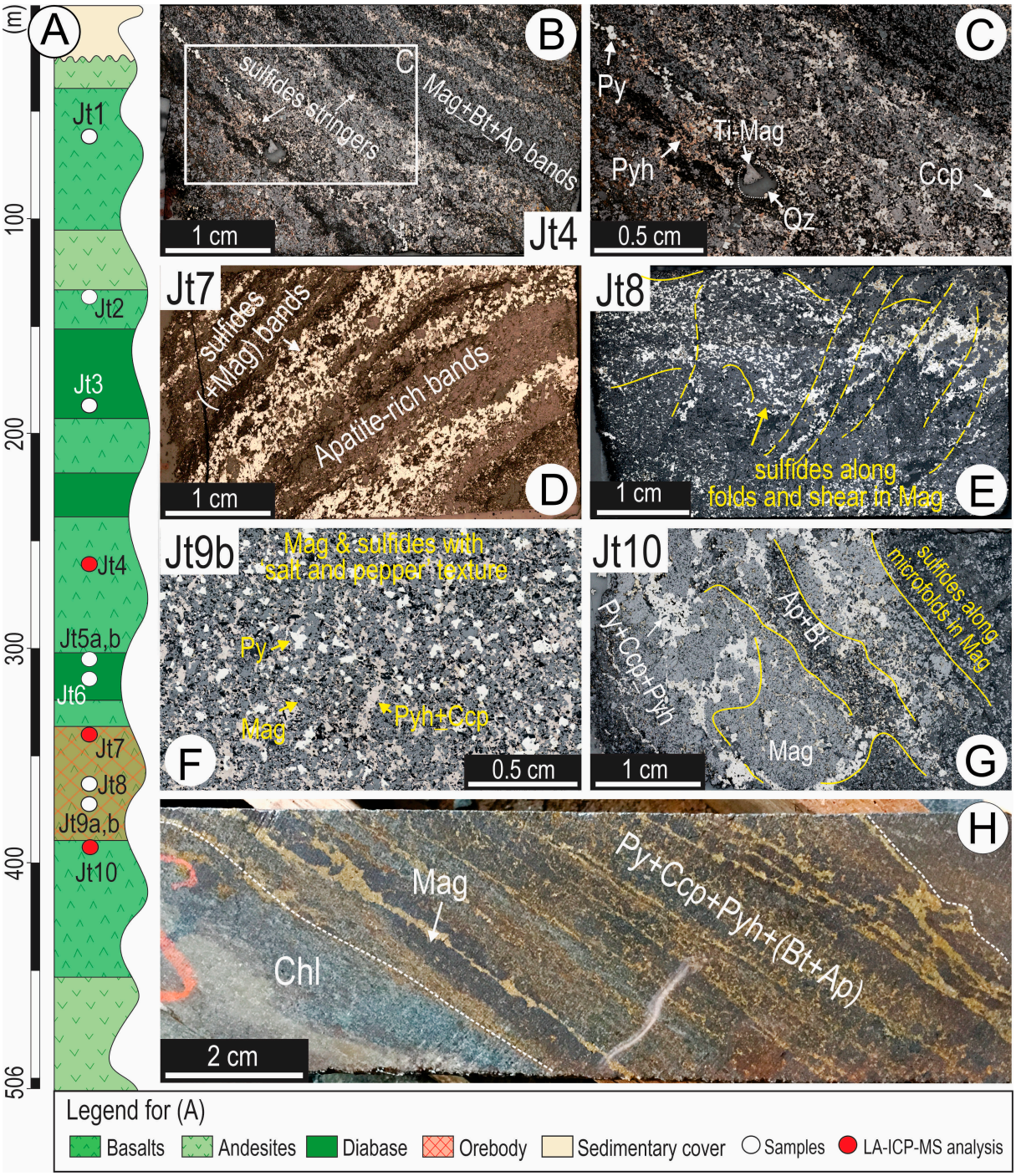

Figure 3. Schematic lithological cross-section of sampled drillhole with sample locations (**A**), reflected light microphotographs (**B**–**G**), and drillcore photograph (**H**). (**B**–**H**) show styles of sulfide mineralization and rock fabrics as labeled and described in the main text. Abbreviations: Ap—apatite; Bt—biotite; Ccp—chalcopyrite; Chl—chlorite; Mag—magnetite; Py—pyrite; Pyh—pyrrhotite; Qz—quartz. Image in (**H**) is from lower part of the drillhole.

Outside the magnetite-dominant orebody, notably in sample Jt4, the sulfides occur as disseminations, stringers, and bands following the rock fabrics (Figure 3B). Sulfide stringers are present within bands intercalated with magnetite + apatite + biotite within metabasalts. There is no close relationship between the sulfides, dominantly pyrrhotite and pyrite, and magnetite (Figure 3C).

In contrast, samples from the orebody display an intimate association with magnetite. Centimeter-sized bands of sulfides + magnetite are intercalated with apatite-rich bands (Figure 3D). The sulfides follow the folding and microshearing of magnetite (Figure 3E). A characteristic 'salt-and-pepper' texture comprising fine-grained sulfides and magnetite is found in pockets of massive ore (Figure 3F). At the lower contact of the orebody with host rocks, sulfides are concentrated as coarser (mm-sized) pods following microfolding within host magnetite (Figure 3G).

Throughout the drillhole, the most prominent fabric displayed by sulfides is that of fine-stringers and bands that follow a mylonitic foliation across magnetite-rich intervals alternating with gangue minerals (Figure 3H).

4.1. Ore Petrography and Mineralogy

The sulfide assemblage across the roughly 50 m-thick interval of magnetite-bearing rocks at Jatobá is composed of pyrite and pyrrhotite, with subordinate amounts of chalcopyrite and minor pentlandite (Figure 4). The proportions of minerals vary significantly, with the sulfides + magnetite assemblage making up to ~60% of the rock. Pyrrhotite and chalcopyrite are dominant in pockets of massive ore (e.g., sample Jt9b) where they are intergrown with or interstitial to magnetite (Figure 4A). We note the abundance of pentlandite [$(Fe,Ni)_9S_8$] as short 'flames' throughout pyrrhotite, indicative of exsolution from monosulfide $(Fe,Ni)_{1-x}S$ solid solution. Pyrrhotite is also present as tiny inclusions within magnetite. Other ore minerals are abundant magnetite (locally 30–50% of the rock) and minor ilmenite. The boundaries between sulfides and magnetite are sealed by apatite and clusters of fibrous silicates (mainly biotite, chlorite, and actinolite). Details of pentlandite forming relatively coarser segregations (10–50 μm-sized grains) in pyrrhotite are illustrated in Figure 4B,C. Otherwise, pyrrhotite appears homogeneous, excluding minor fracturing, polishing pits, and incipient alteration to oxides.

Pyrrhotite commonly co-exists with pyrite, although it is only present in minor amounts in samples with banding or stringer fabrics where an enrichment in pyrite relative to other minerals is observed. In most cases, no apparent zoning is observed in pyrite under reflected light. Some pyrite grains have a mottled appearance due to dense, fine inclusions of different types (Figure 4D). The boundaries between sub-grains within aggregates of finer (20–50 μm) pyrite grains outside the orebody are infilled by chalcopyrite (Figure 4E). The mutual 120° triple junctions between the pyrites in such cases represent foam textures, indicative of equilibrium recrystallization or slow cooling and annealing. Scarce sphalerite is noted along trails in pyrite.

Disseminated pyrite in the orebody has variable grain size (50–600 μm) and is often fractured. The grain margins are typically irregular, which is indicative of replacement by assemblages of gangue minerals (e.g., biotite-apatite; Figure 3F). Nonetheless, idiomorphic grain margins are also present, and these likely indicate overgrowths rather than preservation of euhedral habit (Figure 3F, inset). Pockets of pyrite, chalcopyrite, and in some cases, pyrrhotite occur interstitial to magnetite aggregates (Figure 4G,H). Sulfide formation within cavities in magnetite is suggested by the inward growth of pyrite from the magnetite boundary to the center of the pocket, which is infilled by chalcopyrite (Figure 4H). Intimate relationships between chalcopyrite and pyrite (Figure 4I) are observed along the folds and shears in magnetite (Figure 3D). It is not, however, unambiguously clear whether chalcopyrite replaces pyrite or whether the latter forms new crystals growing within dilational jogs. Chalcopyrite can form pockets without other sulfides and, in such cases, is crosscut by sets of thin (<30 μm) needles of silicates (associations of actinolite, biotite, and chlorite) (Figure 4J).

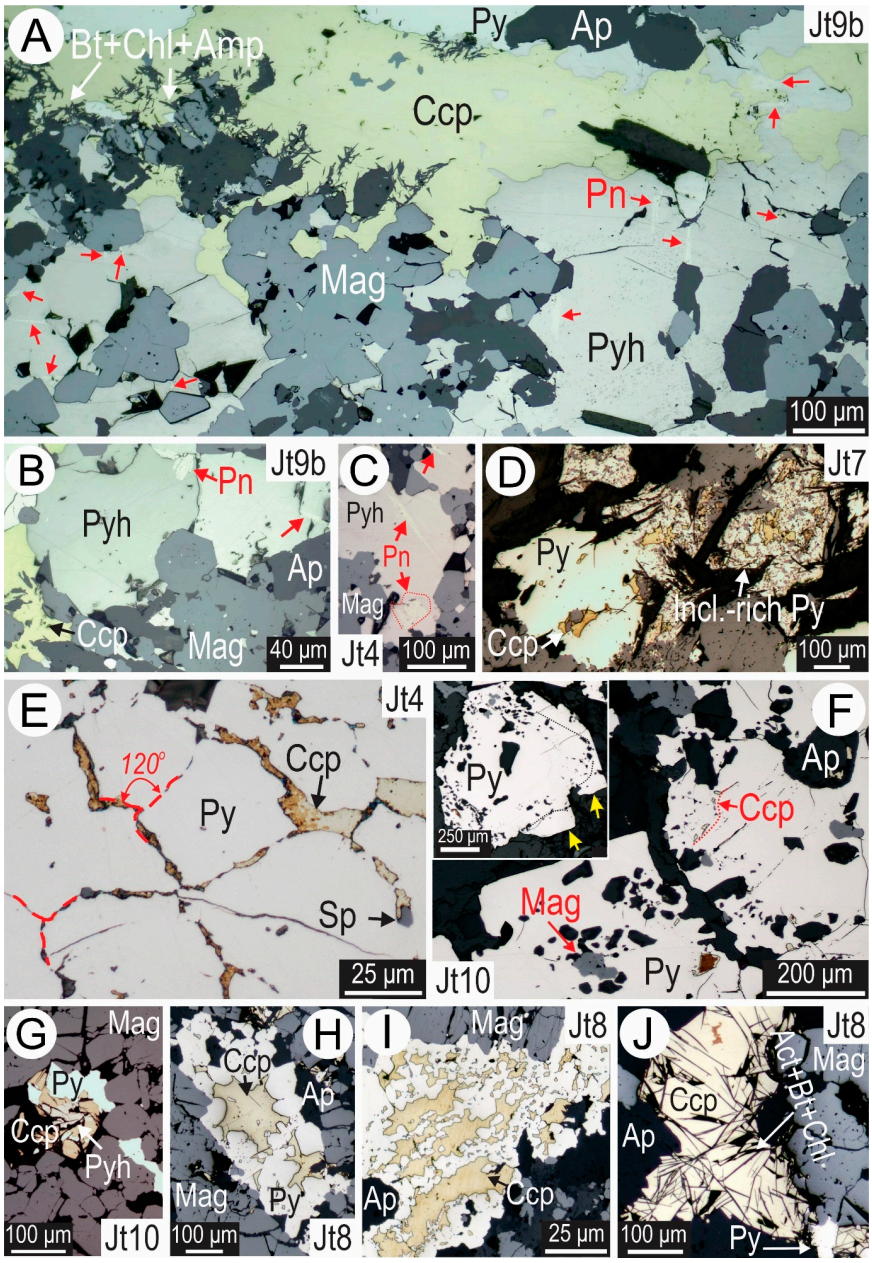

Figure 4. Reflected light images showing sulfide assemblages in the Jatobá samples as labeled. (**A**) Core sample exhibiting banded sulfide mineralization, comprising pyrite (Py), pyrrhotite (Pyh), chalcopyrite (Ccp), and flame-like exsolutions of pentlandite (Pn, red arrows) within a gangue assemblage of magnetite (Mag), biotite (Bt), chlorite (Chl), amphibole (Amp), and apatite (Ap). (**B**,**C**) Pentlandite forming 10–50 µm-sized segregations (grains) in pyrrhotite. (**D**) Pyrite-chalcopyrite assemblage in which the pyrite has a mottled appearance due to dense, fine inclusions of different types. (**E**) Characteristic foam-textured pyrite with 120° triple junctions. Chalcopyrite infills some fractures; minor sphalerite (Sp) is noted along pyrite sub-grain boundaries. (**F**) Pyrite grain margins are irregular and often cuspate, suggestive of replacement. Preserved idiomorphic grain margins (**F** inset) may indicate overgrowths. (**G**) Pyrite interstitial within magnetite associated with pyrrhotite and chalcopyrite. (**H**) Pyrite containing irregular and variably sized inclusions of fluorapatite, magnetite, and chalcopyrite close to the grain margin. Note the curvilinear margins of pyrite against chalcopyrite. (**I**) Extensive replacement of pyrite by chalcopyrite in contact with chlorite, magnetite, and fluorapatite. (**J**) Chalcopyrite overprinted by acicular actinolite (Act).

4.2. Accessory Ore Minerals

A range of Co-, As-, Ni-, and PGE minerals are found throughout the sulfide assemblages (Figure 5). In sulfide-poor samples such as those from the upper part of the sampled interval (sample Jt1), the margins between pyrite and chalcopyrite are marked by small grains of a Co-As-bearing mineral, likely cobaltite (CoAsS; Figure 5A).

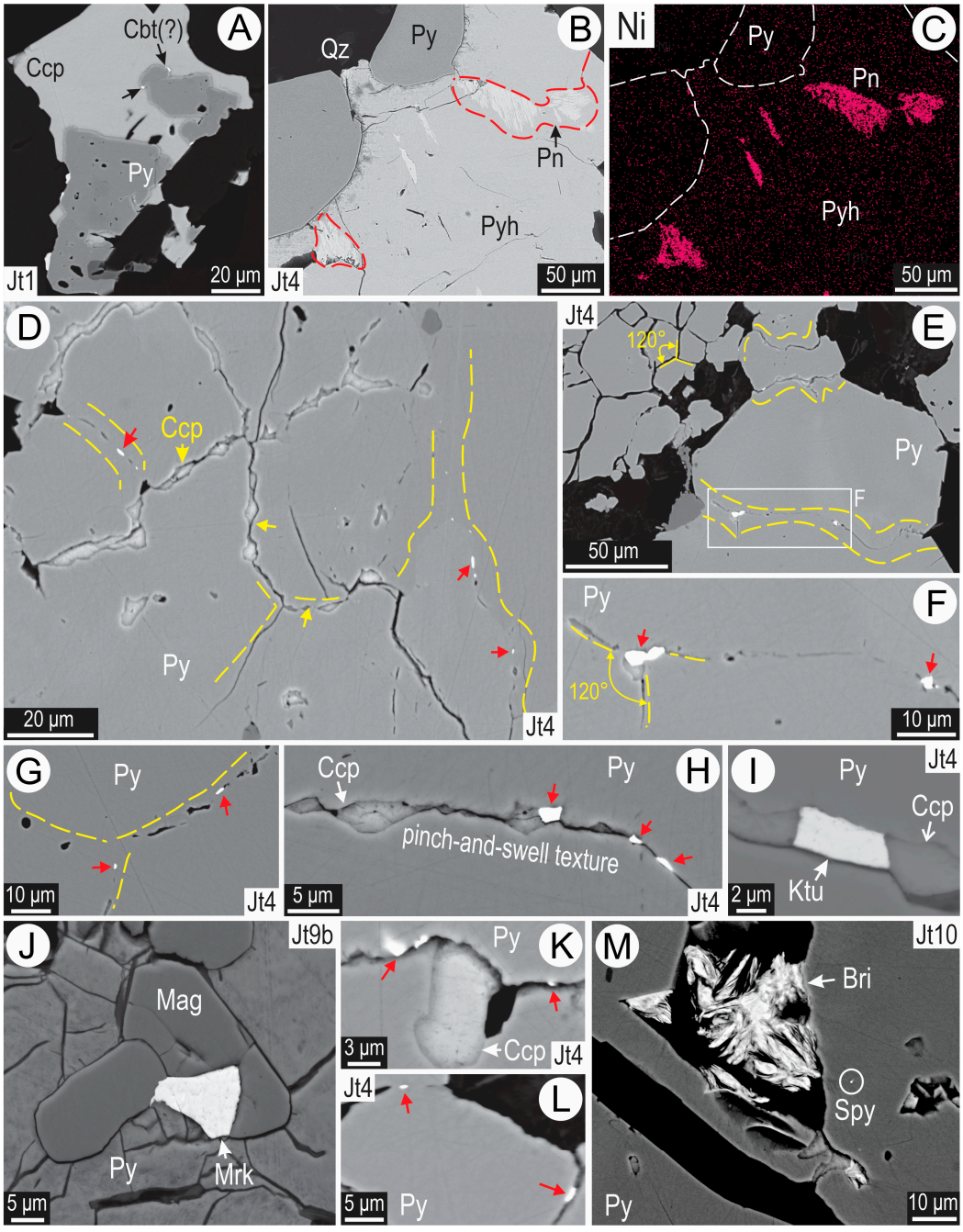

Figure 5. BSE images (except C, EDS element map) showing details of sulfide assemblages in Jatobá samples as labeled. (**A**) Fine cobaltite (Cbt, black arrows) at boundary between pyrite and chalcopyrite. (**B**) Rounded (milled) pyrite enclosed by pyrrhotite. Note the relative abundance of pentlandite lamellae close to grain and sub-grain boundaries. (**C**) EDS element map showing distribution of Ni in area imaged in B, highlighting the pentlandite lamellae. (**D**) Characteristic foam-textured pyrite with remobilized chalcopyrite located along pinch-and-swell fractures (yellow arrows), which also host tiny PGM inclusions (red arrows). (**E**–**G**) Pyrite displaying indentation with curvilinear boundaries and 120° triple-junctions and PGM inclusions (red arrows). (**H**,**I**) Nucleation and coarsening of chalcopyrite

chalcopyrite and PGM occur along pinch-and-swell textures in foam-textured pyrite are typical of the stringer sulfides in sample Jt4. (**J**) Coarser inclusions of PGM at grain boundaries between magnetite and pyrite in ore zone sample. (**K**,**L**) PGM inclusions associated with gangue biotite, apatite, and quartz along the trails or close to grain boundaries and large pores in pyrite. (**M**) Pore-filled aggregate of britholite-(Ce) within pyrite. Circle highlights sub-micron-sized PGM inclusions adjacent to the pore. Abbreviations: Bri—britholite-(Ce); Cbt—cobaltite; Ccp—chalcopyrite; Ktu—kotulskite; Mag—magnetite; Mrk—merenskyite; Py—pyrite; Pyh—pyrrhotite; Spy—sperrylite.

In stringer sulfides outside the magnetite-rich orebody represented by sample Jt4, the heterogeneous distribution of pentlandite, with coarser segregations towards grain and sub-grain boundaries in pyrrhotite, suggests remobilization of this mineral (Figure 5B,C). The rounded morphology of the pyrite along margins adjacent to pyrrhotite suggests an episode of grain milling of refractory pyrite followed by remobilization of more ductile pyrrhotite. Pentlandite lamellae are most abundant close to grain and sub-grain boundaries in the pyrrhotite. Sulfide textures featuring abundant but small PGM inclusions in foam-textured pyrite are typical of the stringer mineralization (Figure 5D–I).

Remobilization of chalcopyrite, the most ductile among sulfide minerals, along pinch-and-swell fractures in pyrite is not only common but is accompanied by the nucleation of tiny PGE-bearing minerals (Figure 5D). In closer detail, the pyrite grains show indentation with curvilinear boundaries and 120° triple-junctions, many of which are marked by the presence of tiny grains of platinum-group minerals (PGM) (Figure 5E–G). Nucleation and coarsening of chalcopyrite and PGM occur along the pinch-and-swell textures (Figure 5H,I).

In contrast, sulfides from the orebody include somewhat larger inclusions of PGM (up to 20 μm), some of which are located interlocked at grain boundaries between magnetite and pyrite (Figure 5J). Moreover, these PGM inclusions are associated with gangue minerals (e.g., biotite, apatite, quartz) along the trails or close to grain boundaries, as well as in large pores in pyrite from the orebody samples (Figure 5K–M). Britholite-(Ce), $(Ce,Ca)_5(SiO_4)_3OH$, and uraninite are conspicuous components of assemblages formed within such pores. Aggregates of britholite-(Ce) are seen infilling some of the larger pore spaces (Figure 5M). We also note the presence of sub-micron-sized PGM inclusions adjacent to the pore.

Other trace minerals identified in the Jatobá ores include an eclectic range of oxides, sulfides, and rare earth element (REE) phosphates. Titanite is present as sporadic, micron-sized inclusions in magnetite, whereas ferberite and scheelite occur typically as inclusions in ilmenite, either as isolated inclusions or as dense swarms of sub-micron-sized nanograins in the center of the ilmenite. Molybdenite is also found in relatively coarse (tens of microns) yet scarce inclusions in magnetite. Allanite, huttonite or thorite (ThO_2), euxenite-(Y) $[(Y,Ca,Ce,U,Th)(Nb,Ta,Ti)_2O_6]$, and uraninite ($UO_2$) up to 60 μm in size and with inclusions of galena are common and are typically included in magnetite.

4.3. Platinum Group Minerals

Although typically small (0.5 to 10 μm across), the suite of PGM forming inclusions within or otherwise associated with Jatobá pyrite were characterized in terms of their composition and association with one another (Figures 6–8; Table 1).

The PGM phases tentatively identified comprise species from three distinct groups: (i) Pd-Te-Bi compounds, merenskyite [(Pd,Pt,Ni)(Te,Bi)], kotulskite, $[Pd(Te,Bi)_{2-x}]$, and michenerite (PdBiTe)]; (ii) compounds of Pd with Sb, borovskite (Pd_3SbTe_4), naldrettite (Pd_2Sb), and sudburyite (PdSb); and (iii) Pt-As compounds, notably sperrylite ($PtAs_2$). Despite their small size, empirical formulae could be calculated for merenskyite, by far the most common PGM with variable Ni and Bi contents, and for naldrettite (Table 1).

Merenskyite occurs as single-phase thin slivers (Figure 6A–C), blebby grains (Figure 6D), or as binary inclusions together with kotulskite (Figure 6E). Other relatively large (5 μm-sized) inclusions occurring as single phases are kotulskite, sudburyite, and naldrettite (Figures 6F,G and 7B,C). Micron-sized native gold (97.9% Au) is also observed within pyrite from the orebody, as is native bismuth. (Figure 6H,I).

Analysis and EDS mapping of a grain of merenskyite located at the boundary between pyrite and magnetite (Figure 7A) yields the empirical formula $(Pd_{0.83}Ni_{0.12}Pt_{0.07})_{1.02}(Te_{1.69}Bi_{0.29})_{1.98}$ (analysis 3 in Table 1), consistent with the tendency of this mineral to incorporate significant concentrations of Pt and Ni substituting for Pd and of Bi substituting for Te. The brighter patch within the grain gives ~PdBiTe (michenerite?) (Figure 7A). Sperrylite and borovskite were identified from some of the smallest inclusions, for which EDS spectra are shown in Figure 8.

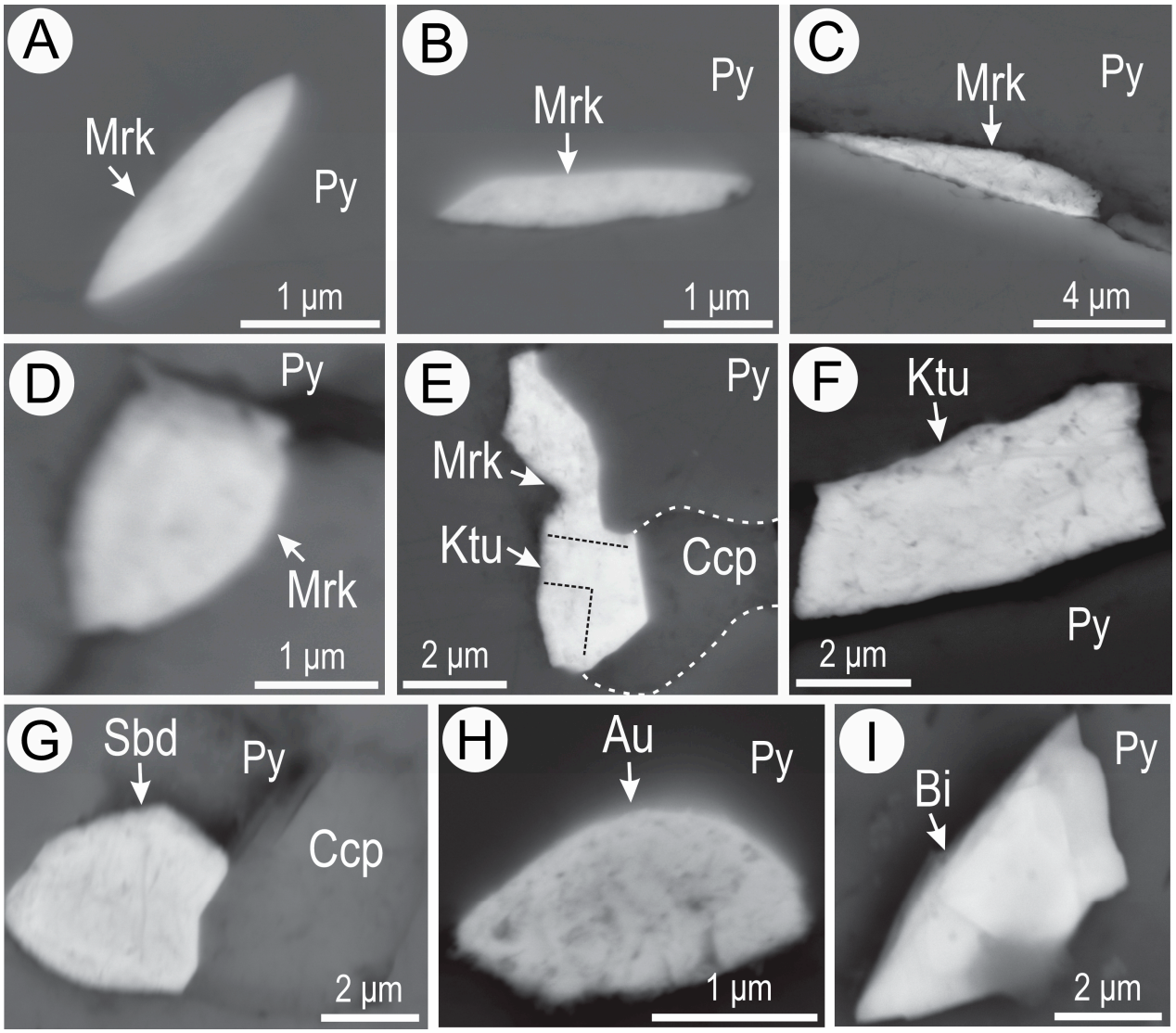

Figure 6. BSE images showing sulfide assemblages containing PGM. (**A**–**C**) Lozenge-shaped inclusions of merenskyite (Mrk) within pyrite (Py). (**D**) Merenskyite located at a triple junction within pyrite aggregate. (**E**) Two-phase inclusion of merenskyite and kotulskite (Ktu) within pyrite. (**F**) Grain of kotulskite within a fracture in pyrite. (**G**) Rounded bleb of sudburyite (Sbd) with chalcopyrite (Ccp) along a microfracture in pyrite. (**H**) Sub-rounded bleb of native gold (Au) within pyrite. (**I**) inclusion of native bismuth (Bi).

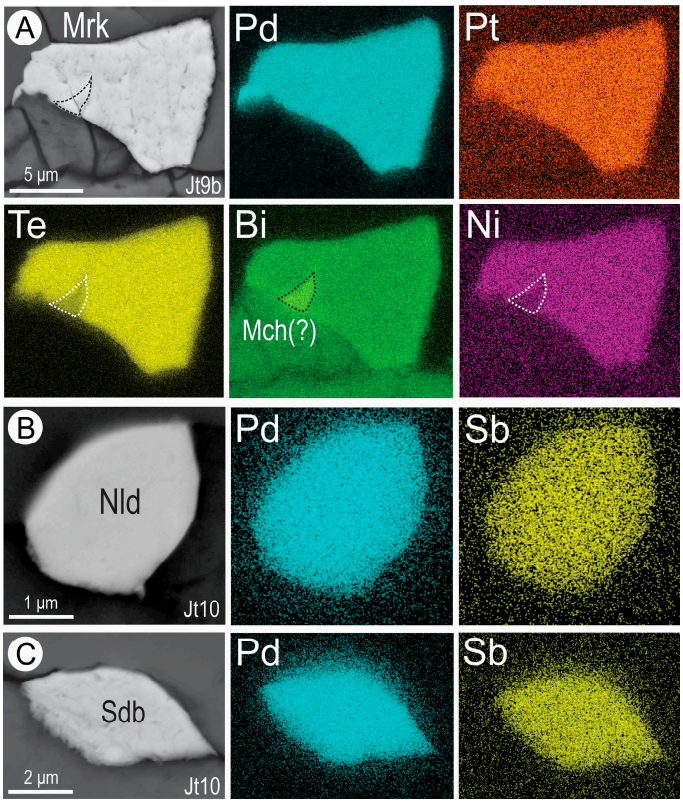

Figure 7. BSE images and respective EDS element maps for selected elements in (**A**) relatively coarse grain of merenskyite (Mrk) at pyrite-magnetite boundary, with brighter patch corresponding to michenerite (Mch), (**B**) naldrettite (Nld) within pyrite, and (**C**) sudburyite (Sdb) within pyrite.

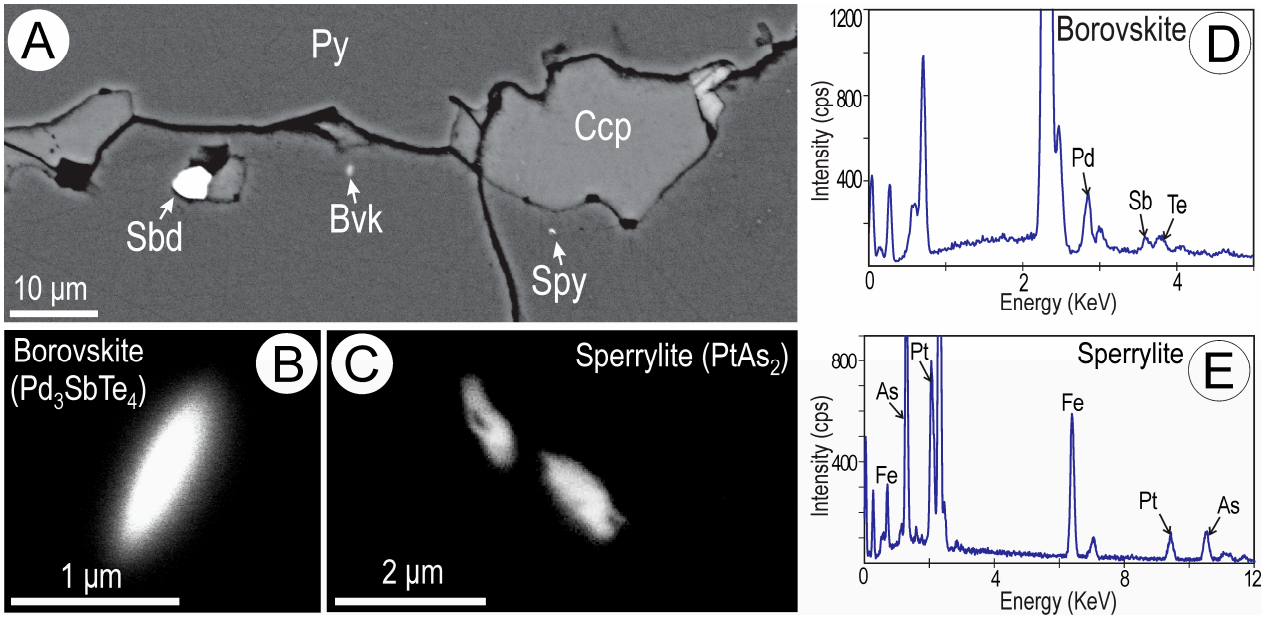

Figure 8. (**A**) Fracture in pyrite (Py) containing chalcopyrite (Ccp) and inclusions of Pd-Pt minerals including borovskite (Bvk), sudburyite (Sdb), and sperrylite (Spy). (**B**,**C**) High-magnification images of borovskite and sperrylite, respectively. (**D**,**E**) EDS spectra supporting identification of sub-micron-sized inclusions shown in B and C.

4.4. Trace Element Concentrations in Sulfides

Trace element concentrations in Jatobá pyrite are summarized in Table 2 and shown on box-and-whisker plots in Figure 9. The full dataset is provided in Supplementary Materials Table S1. Concentration ranges are relatively wide for Ni (~10 to ~1000 ppm) and As (<1 to ~1000 ppm). Cobalt also shows concentration ranges across four orders of magnitude (<10 to >20,000 ppm). Selenium concentrations are typically a couple of hundred ppm. These elements all give smooth signals on time-resolved LA-ICP-MS depth profiles (Figure 10). Other trace elements such as Cu, Bi, Sb, and Te yield irregular signals and are thus considered largely inclusion bound.

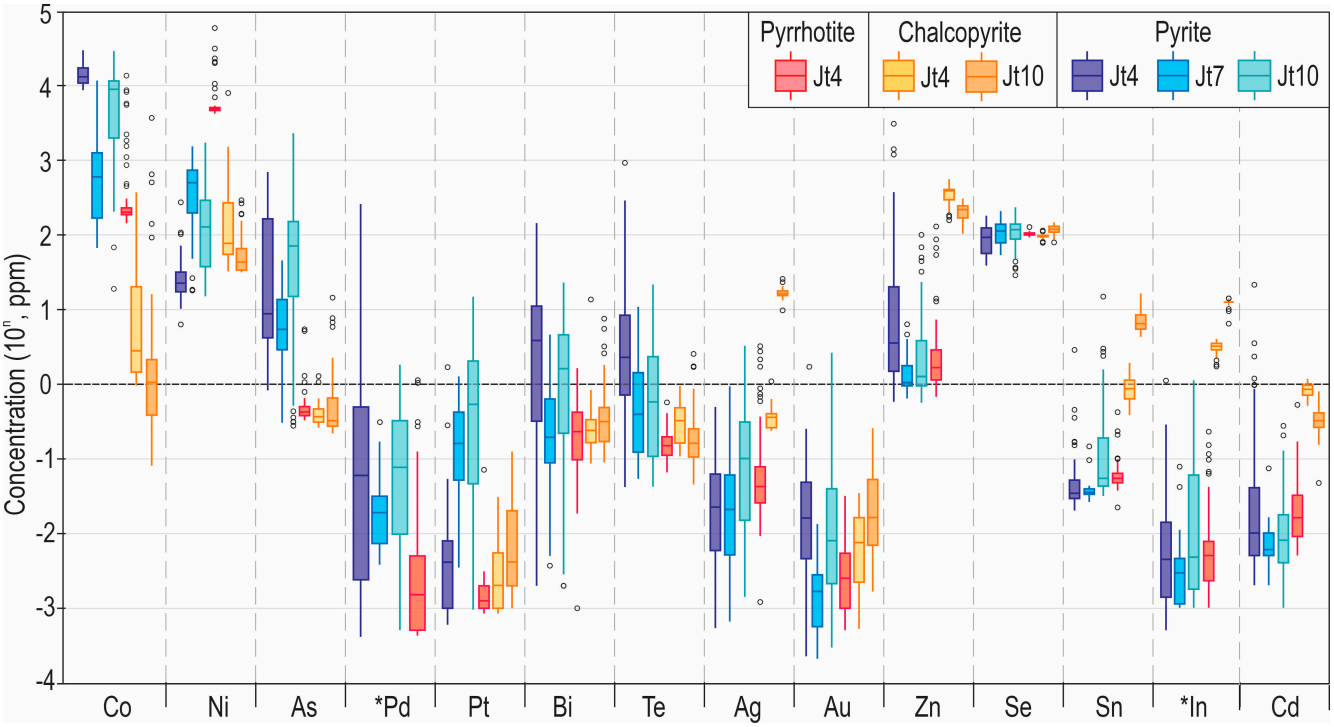

Figure 9. Box-and-whisker plots comparing the concentrations of thirteen key trace elements in pyrite from three different samples, as well as in chalcopyrite (in two samples) and pyrrhotite. *Pd refers to mean Pd calculated based on ^{105}Pd and ^{106}Pd, and *In refers to the calculated mean for concentration of ^{113}In and ^{115}In.

There is a variability in the concentration ranges of Co, Ni, and As across pyrite in different samples. Although part of this variability is due to grain-scale compositional zoning, we draw attention to differences in the measured concentrations of Pd (mean 7.4 ppm in sample Jt4 but <1 ppm in samples Jt7 and Jt10) and Pt (mean 1.7 ppm in Jt10, and <1 ppm in Jt7 and Jt4). We note that the highest Pd is measured in pyrite from sample Jt4, whereas the highest Pt is from sample Jt10. Neither Pd nor Pt correlates with Cu, Zn, or other elements and thus are interpreted as genuine and not an artefact of mass interference from argides.

Table 2. Summary of LA-ICP-MS trace element data for Jatobá sulfides (in ppm).

Pyrite Jt 4	**Co**	**Ni**	**Cu**	**As**	**Zn**	**Bi**	**Te**	**Au**	**Ag**	**Se**	**Cd**	***In**	**Sb**	**Sn**	**ΣPb**	**^{105}Pd**	**^{106}Pd**	***Pd**	**Pt**
Mean (n = 56)	14,532	33	2002	99	136	12	31	0.060	0.054	97	0.585	0.043	0.336	0.108	5.1	8.7	6.1	7.4	0.043
S.D.	4823	38	8203	167	473	24	131	0.230	0.091	40	2.9	0.155	0.570	0.378	6.9	43	26	35	0.228
Median	13,104	23	6.0	8.8	3.6	3.9	2.3	0.008	0.023	97	0.010	0.004	0.102	0.034	1.9	0.033	0.027	0.033	0.004
Maximum	29,711	273	57,218	697	3080	144	923	1.7	0.497	187	21.1	1.1	2.8	2.8	32	311	181	246	1.7
Minimum	8666	6.3	0.225	0.828	0.582	<0.002	<0.042	0.001	<0.001	40	0.002	0.001	0.004	0.02	0.008	0.001	0.001	0.000	<0.001
Pyrite Jt 7																			
Mean (n = 29)	2441	546	78	11	1.7	0.613	1.2	0.002	0.082	116	0.009	0.007	0.397	0.041	3.0	0.046	0.041	0.044	0.294
S.D.	3799	419	90	13	1.4	0.972	2.1	0.003	0.188	40	0.013	0.016	0.476	0.023	3.9	0.077	0.064	0.070	0.329
Median	599	500	292	5.4	1.1	0.195	0.395	0.001	0.021	116	0.006	0.003	0.149	0.035	1.3	0.016	0.015	0.018	0.161
Maximum	11,669	1533	0.9	45	6.4	4.6	11	0.013	0.937	211	0.073	0.078	1.6	0.144	12	0.362	0.266	0.314	1.3
Minimum	67	18	1450	<0.305	0.645	0.004	<0.054	0.001	<0.001	55	0.002	0.001	0.012	0.026	0.010	0.001	0.001	0.000	0.004
Pyrite Jt 10																			
Mean (n = 99)	8012	229	1371	181	6.0	3.5	1.8	0.051	0.351	116	0.021	0.092	0.575	0.381	6.6	0.247	0.223	0.235	1.7
S.D.	5766	291	3413	400	14	4.7	2.9	0.266	0.620	40	0.041	0.205	0.662	1.5	10	0.358	0.348	0.350	2.8
Median	8912	128	7.9	71	1.3	1.6	0.580	0.006	0.101	119	0.008	0.005	0.285	0.054	2.8	0.081	0.077	0.076	0.489
Maximum	28,916	1721	19,113	2302	100	23	22	2.6	3.3	238	0.272	1.1	2.8	15	51	1.8	1.8	1.8	15
Minimum	19	15	0.156	<0.278	0.563	<0.002	<0.043	0.001	<0.001	30	0.001	0.001	0.010	0.031	0.010	0.001	0.001	0.001	<0.001
Pyrrhotite Jt4	**Co**	**Ni**	**Cu**	**As**	**Zn**	**Bi**	**Te**	**Au**	**Ag**	**Se**	**Cd**	***In**	**Sb**	**Sn**	**ΣPb**	**^{105}Pd**	**^{106}Pd**	***Pd**	
Mean (n = 61)	981	12,023	961	0.620	7.9	0.315	0.177	0.004	0.254	106	0.033	0.017	0.033	0.067	6.4	0.059	0.045	0.052	
S.D.	2403	23,152	5996	0.885	22	0.333	0.098	0.006	0.634	6.2	0.069	0.039	0.043	0.056	11	0.238	0.166	0.200	
Median	201	4899	2.1	0.426	1.7	0.232	0.151	0.001	0.043	106	0.016	0.005	0.021	0.054	3.2	0.001	0.001	0.001	
Maximum	13,582	11,5245	45,434	5.4	129	1.6	0.571	0.032	3.2	131	0.520	0.228	0.288	0.415	68	1.5	0.968	1.1	
Minimum	143	20	0.433	0.328	0.680	<0.001	<0.065	0.001	<0.001	95	0.005	0.001	<0.005	0.022	0.037	0.001	0.001	0.000	
Chalcopyrite Jt 4	**Co**	**Ni**	**Cu**	**As**	**Zn**	**Bi**	**Te**	**Au**	**Ag**	**Se**	**Cd**	***In**	**Sb**	**Sn**	**ΣPb**				**Pt**
Mean (n = 23)	28	538		0.447	348	0.861	0.365	0.011	0.380	100	0.826	3.0	0.061	0.932	11				0.005
S.D.	77	1643		0.251	102	2.8	0.231	0.010	0.183	7.2	0.175	0.609	0.052	0.408	10				0.008
Median	2.8	77		0.368	390	0.240	0.326	0.006	0.361	99	0.840	3.2	0.035	0.856	6.9				0.002
Maximum	372	7943		1.3	557	14	0.950	0.035	1.1	113	1.2	4.0	0.233	1.9	40				0.031
Minimum	0.956	32		<0.262	157	0.087	0.108	<0.001	0.237	86	0.504	1.7	0.018	0.381	1.6				<0.001
Chalcopyrite Jt 10																			
Mean (n = 45)	114	68		1.2	206	0.755	0.330	0.044	17	121	0.337	12	0.084	7.3	15				0.015
S.D.	558	60		2.6	52	1.4	0.496	0.063	2.6	17	0.135	1.3	0.091	2.9	11				0.026
Median	1.1	43		0.325	218	0.316	0.162	0.013	16	123	0.320	12	0.045	6.4	13				0.003
Maximum	3686	291		14	306	7.6	2.5	0.258	26	151	0.788	15	0.383	16	48				0.125
Minimum	0.081	32		<0.219	104	0.090	<0.046	0.001	10	86	0.047	6.4	<0.011	4.2	1.6				<0.001

Note: ^{105}Pd and ^{106}Pd refer to calculated total Pd concentration calculated based on measurement of ^{105}Pd and ^{106}Pd isotope signals, respectively. Mean concentration reported as *Pd. *In refers to the calculated mean for concentration of ^{113}In and ^{115}In. Measurements of Mo, W, and U are consistently below minimum limits of detection.

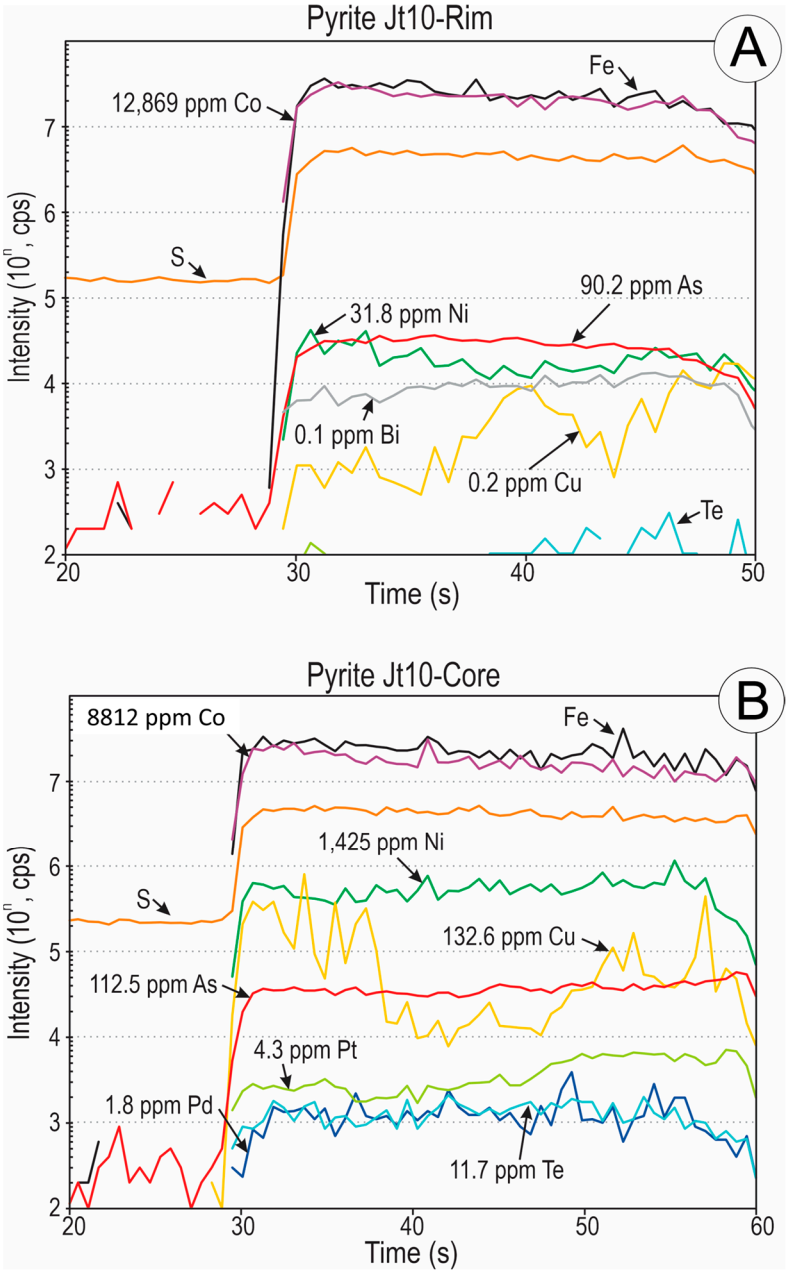

Figure 10. Time-resolved LA-ICP-MS depth profiles for representative pyrite grain in sample Jt10 (rim: (**A**); core: (**B**)). Note the generally flat signals, including for ppm-level Pt and Pd (on (**B**)), but ragged signals for inclusion-hosted elements such as Cu (on (**B**)).

The other main sulfides are also carriers of several trace elements (Table 2). Pyrrhotite contains the highest concentrations of Ni (mean 12,023 ppm, but in part attributable to flames of pentlandite or other impurities), hundreds of ppm Co and Cu (mean 981 and 961 ppm, respectively), and 106 ppm Se. Other elements that are measurable in trace concentrations include Pd (mean 0.059 ppm). Chalcopyrite also concentrates Ni and Co (means 538 and 28 ppm in sample Jt4, and 68 and 114 ppm, respectively, in sample Jt10) as well as Se (100 ppm in sample Jt4 and 121 ppm in sample Jt10). Chalcopyrite also contains the highest Zn (348 and 206 ppm in samples Jt4 and Jt10, respectively) as well as measurable concentrations of In (6.1 ppm in sample Jt4 and 17 ppm in sample Jt10). Sample Jt10 contains greater concentrations of both Ag (17 ppm) and Sn (7.3 ppm) than sample Jt4.

A series of binary plots for trace elements in the Jatobá sulfides are shown in Figures 11 and 12. A plot of Co vs. Ni is shown for all sulfides in the sample outside the orebody (sample

Jt4) on Figure 11A and in the two samples from the orebody (samples Jt7 and Jt10) in Figure 11B). In sample Jt4, a strong positive correlation (r = 0.86) is seen between Co and Ni in chalcopyrite and pyrrhotite, whereas pyrite forms a separate cluster, rich in Co but poorer in Ni. Pyrite from the orebody shows different clusters for the two samples, partially overlapping with each other, whereas chalcopyrite from sample Jt10 is distinct, with the lowest Co concentrations. Plots of As vs. Co/Ni for pyrite show distinct trends for the stringer and orebody sulfides. A weak negative correlation (r = −0.27) is seen for sample Jt4 (Figure 11C), whereas a reasonably strong positive correlation (r = 0.66) exists in the orebody samples (Jt7 and Jt10; Figure 11D). A strong positive correlation (r = 0.88) is observed between In and Zn across all sulfides in the three samples (Figure 11E). The lower concentration is in pyrrhotite from sample Jt4, and the highest is from chalcopyrite. A plot for In vs. Sn in chalcopyrite shows the strongest positive correlation (r = 0.95), whereby concentrations are lower in sample Jt4 relative to Jt10 (Figure 11F).

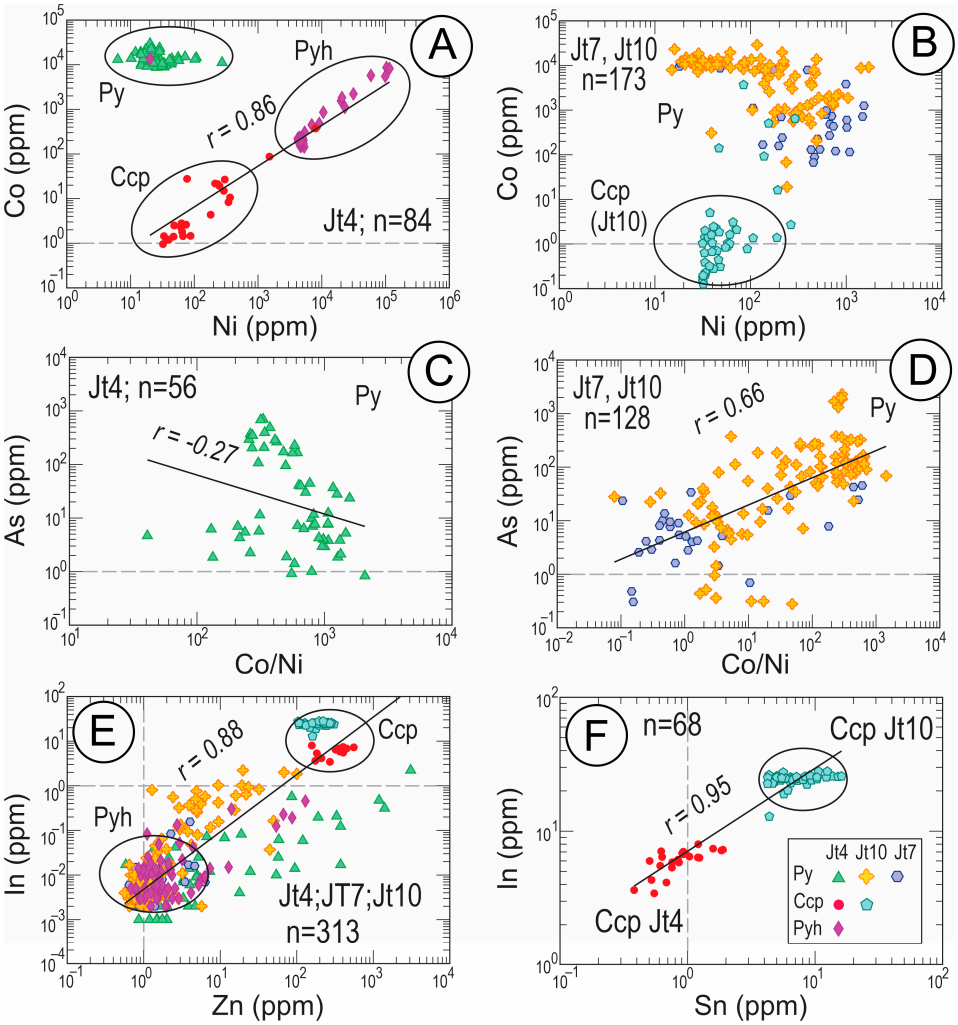

Figure 11. Binary plots of LA-ICP-MS concentration data for selected elements in pyrite and associated sulfides from Jatobá. (**A**,**B**) Ni vs. Co in samples Jt4 (stringer sulfides) and Jt7/Jt10 (ore), respectively. (**C**,**D**) Co/Ni vs. As in sample Jt4 (stringer sulfides) and Jt7/Jt10 (ore), respectively. (**E**) Zn vs. In in various sulfides. (**F**) Sn vs. In in various sulfides.

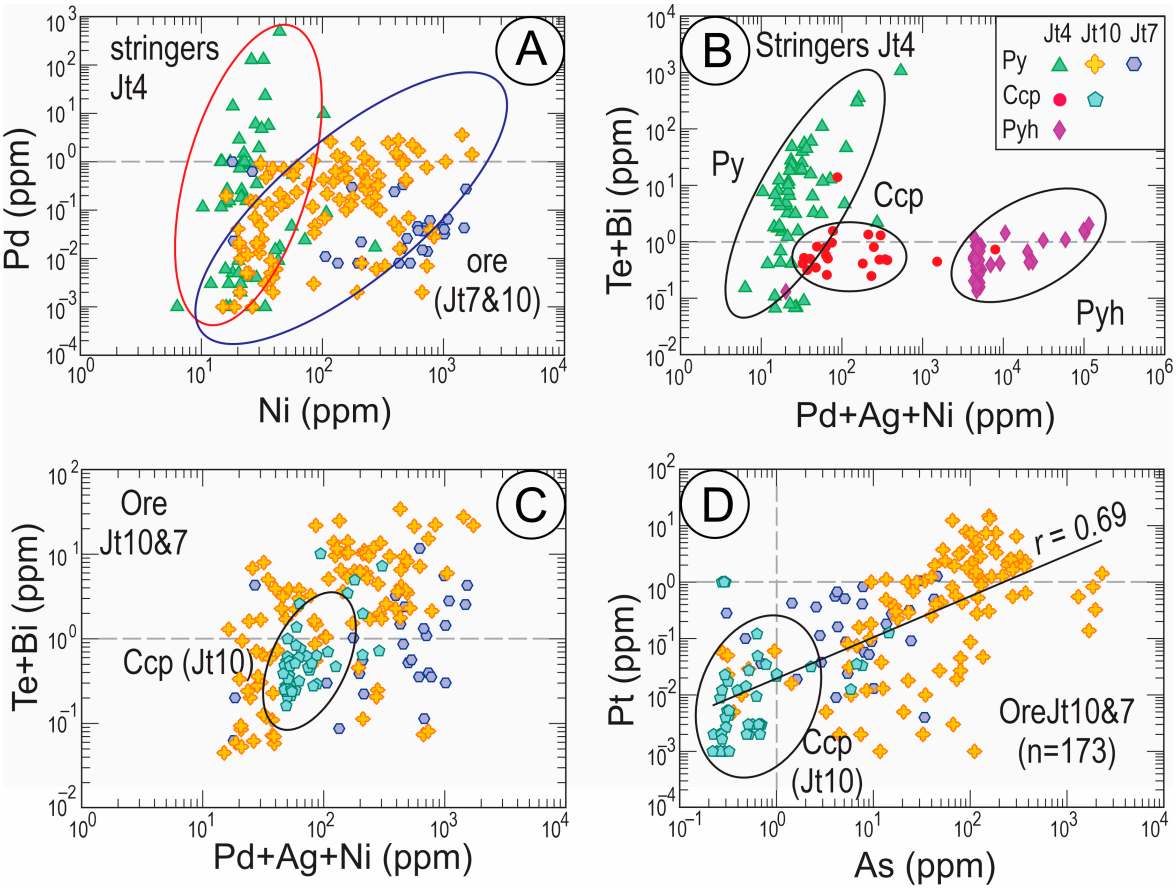

Figure 12. Binary plots of LA-ICP-MS concentration data for selected elements in pyrite and associated sulfides from Jatobá. (**A**) Pd vs. Ni in pyrite (**B**) Pd + Ag + Ni vs. Te + Bi in sulfides from sample Jt4. (**C**) Pd + Ag + Ni vs. Te + Bi in pyrite from the orezone (**D**) As vs. Pt in pyrite. See text for further discussion.

Plots of Pd vs. Ni in pyrite (Figure 12A) also show distinct trends for the stringer sulfides (sample Jt4) relative to orebody samples (Jt7 and Jt10). Combining the data for the three sulfides in sample Jt4 on a plot of (Te + Bi) vs. (Pd + Ag + Ni) (Figure 12B), we show that only pyrite has a positive correlation. This agrees with the presence of merenskyite as the dominant PGM included in pyrite. The same plot for ore samples (Jt7 and Jt10; Figure 12C) shows an undifferentiated cluster (chalcopyrite, also overlapping with pyrite). This is concordant with the wider speciation of PGM in the ore samples. A positive correlation (r = 0.69) is, however, obtained for sulfides in the ore samples if Pt is plotted against As (Figure 12D), agreeing with the presence of sperrylite in these samples.

4.5. Grain-Scale Trace Element Distributions in Pyrite

Compositional zoning is highlighted in three LA-ICP-MS element maps of pyrite (Figures 13–15). Subtle oscillatory zoning with respect to Co and As is observed in a pyrite grain from outside the orebody (sample Jt4; Figure 13). We note that Co is higher at the grain margin, whereas As is concentrated in the core. This is concordant with the plot in Figure 11C. Fractures in pyrite are highlighted by enhanced concentrations of Ni, suggesting this element is leached from the sulfide during brecciation. A homogenous distribution of Se is observed, whereas Pd shows features that somewhat match those shown by Ni. Small, high-concentration spots on the element map for Pd may be attributed to PGM inclusions that nucleated along such fractures.

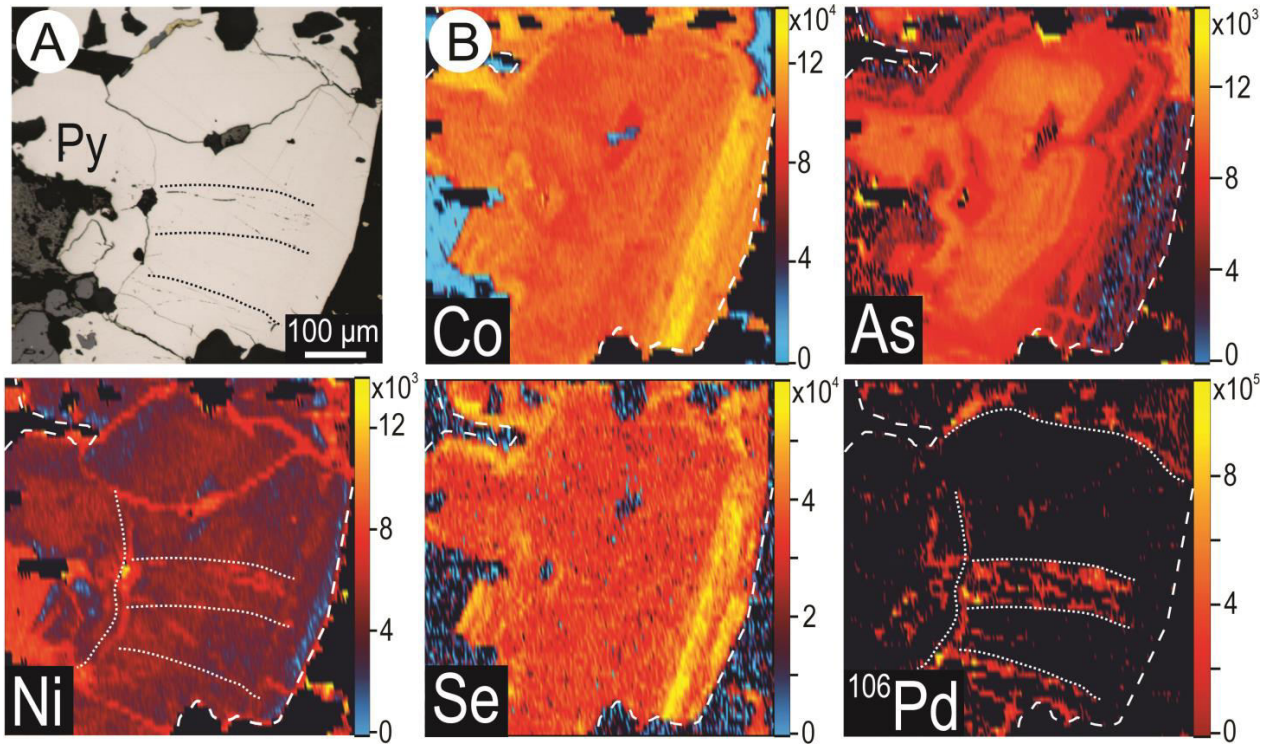

Figure 13. Reflected light image (**A**) and selected LA-ICP-MS element maps (**B**) of a representative pyrite grain from sample Jt4 showing subtle oscillatory zoning with respect to Co and As, in which Co is higher at the grain margin and As is relatively concentrated in the grain core. Open and healed microfractures in pyrite are highlighted on the maps for Ni and, to some degree, also by Pd. The Se map suggests a homogenous distribution across the grain. Small yellow spots of high concentration on the Pd map are attributed to fracture-bound inclusions of PGM. Scales in counts per second.

Element maps of a pyrite grain in orezone sample Jt10 (Figure 14) feature distinct patterns. Annealing of pyrite aggregates is supported by the Co-, Pt-, As-enriched, and Ni-depleted cores of individual sub-grains. We note that, despite the low absolute concentrations of Pt, the Pt element map shows a perfect correlation with the Co-rich grain cores. Cobalt also shows oscillatory zoning highlighting individual grains that form a fused aggregate. Subtle, slightly patchy zoning is depicted by the distribution of Se. Palladium reflects grain boundaries in the annealed aggregate whereas Cu (inclusion of chalcopyrite in the middle of the aggregate) correlates with higher concentrations of Ag, Sn, and to some extent also Bi. The latter is also redistributed along grain boundaries. We note that the map for U also highlights grain boundaries, consistent with our observations of uraninite.

In contrast, fractures and submicron trails of inclusions are shown on the element maps obtained from the margin of a coarser, mm-sized pyrite grain in sample Jt10 (Figure 15). A subtle oscillatory zoning with respect to Co, Se, and Pt is depicted on the respective maps, whereas As is relatively homogenous across the mapped area except for a small domain of high concentration. Sets of parallel fractures are highlighted by the relative enrichment of Ni, Pd, Ag, and Sb, fully consistent with our observations of micron-sized phases in which Pd is combined with these elements. Other inclusions, comprising U-, Se-, and Mn-bearing minerals, are also picked out in the pyrite.

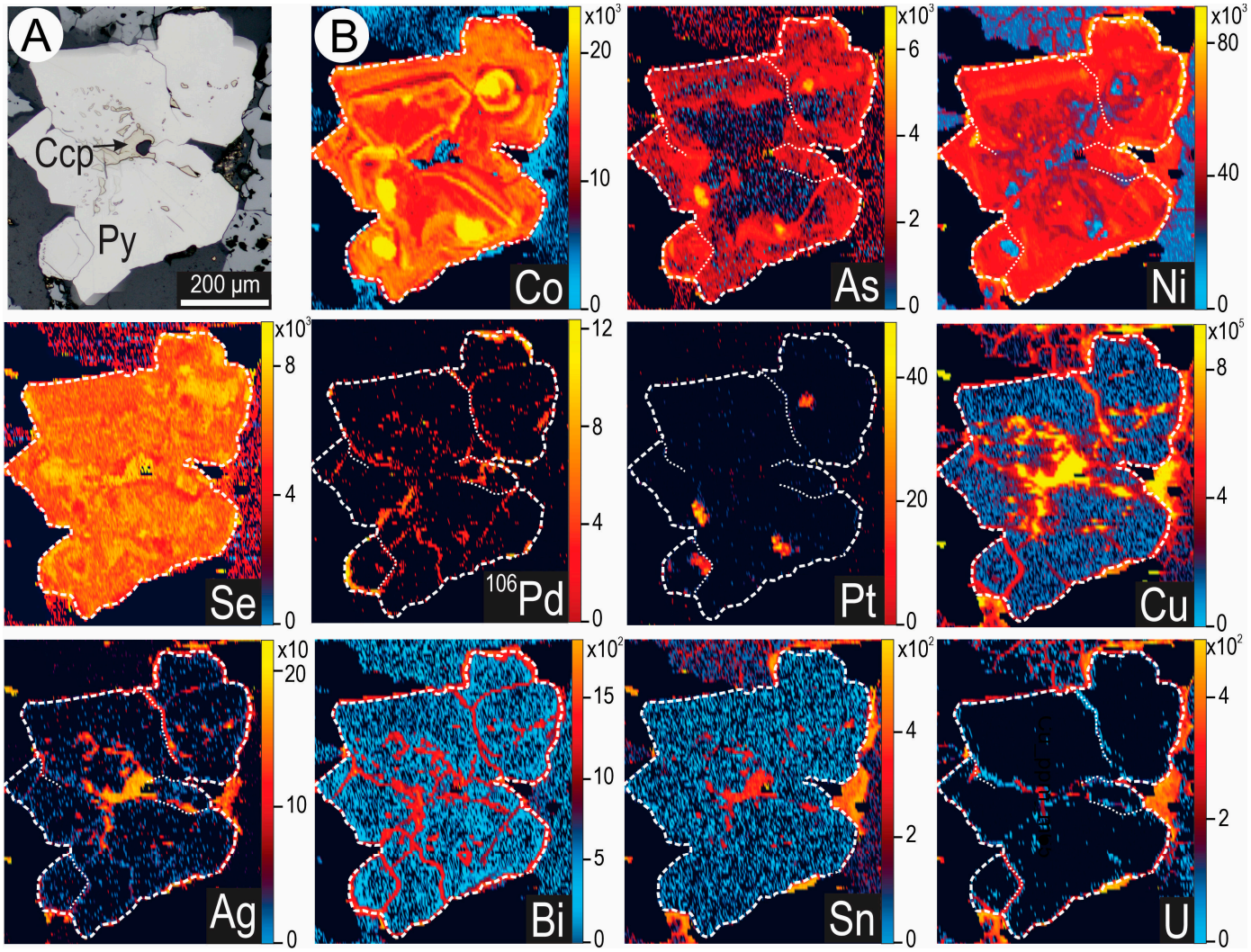

Figure 14. Reflected light image (**A**) and selected LA-ICP-MS element maps (**B**) of a representative pyrite grain from sample Jt10. Maps for Co, Pt, As, and Ni indicate annealing of a multi-grain pyrite aggregates in which individual grain cores can be picked out, notably on the Co map. Pt distributions correlate strongly with those of Co. Pd distributions and reflect grain boundaries in the annealed aggregate. Cu distributions correspond to inclusions of chalcopyrite, which are also picked out on the Ag, Sn, and Bi maps. Maps for Ag, Bi, and U also highlight the sub-grain boundaries. Scales in counts per second. Py—pyrite; Ccp—chalcopyrite.

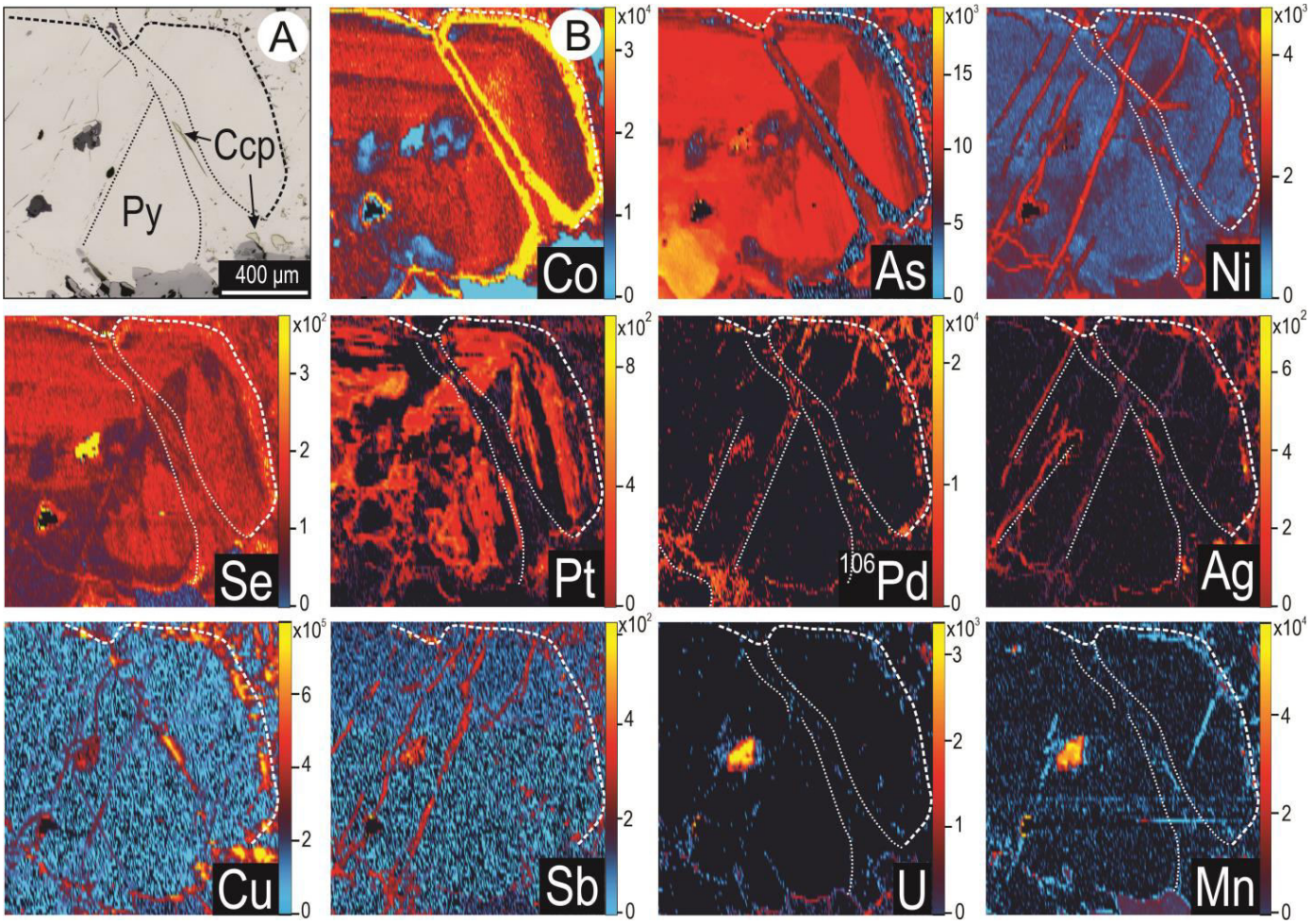

Figure 15. Reflected light image (**A**) and selected LA-ICP-MS element maps (**B**) of the margin of a coarser pyrite grain in sample Jt10. The maps define subtle oscillatory zoning (Co, Se, and Pt) fractures and submicron trails of inclusions and sets of parallel fractures highlighted by the relative enrichment of Ni, Pd, Ag, and Sb. Py—pyrite; Ccp—chalcopyrite.

5. Discussion

5.1. Origin, Trace Element Signatures, and Successive Generations of Jatobá Sulfides

The orebody studied from Jatobá is associated with magnetite + apatite rich assemblages that are interpreted to be of IOCG affiliation. The Ni-bearing character of the sulfide assemblages was recognized by Veloso et al. [20], who considered 'Ni-pyrrhotite and Ni-pyrite' to be the main phases and that they represented the first stage of mineralization that introduced Ni into the system. Veloso et al. [20] explained the formation of Ni-mineralization in the context of a deep, evolving IOCG system at the transition between an initial magmatic stage and a subsequent stage termed 'magmatic-hydrothermal' to infer the high temperature of early fluids. In this model, magnetite-apatite associations formed first in an IOA deposit-like scenario, enabling hot, Cl-rich, saline fluids to leach Ni from mafic-ultramafic rocks. According to Veloso et al. [20], such fluids would transport and discharge episodically, resulting in a concentration of the Ni-bearing sulfide ores in the deeper part of the Jatobá ore zones.

The present study shows that sulfides also occur outside of the magnetite-rich orebody and form stringer zones throughout the mafic host rocks, which are similarly metamorphosed, deformed, and hydrothermally altered (Figure 3). Although the mineral associations within and outside the orebody are essentially similar (pyrrhotite + chalcopyrite + pyrite, in addition to dominant magnetite), the relative proportions of these components vary considerably, with the orebody featuring a greater volume of pyrite than other sulfides.

Pyrrhotite is also a key mineral. It contains pentlandite with only negligible Co content and is closely associated with chalcopyrite (Figure 4) both within and outside the orebody. Apart from pentlandite, pyrrhotite contains the most Ni (Figure 9). By virtue of its greater relative abundance, at least in our samples, pyrite is likely the major Ni carrier in the deposit, followed by pyrrhotite.

Apart from being a Ni carrier, pyrite is also markedly enriched in Co, much more so than the co-existing pyrrhotite (Figure 9). Textures between pyrite and pyrrhotite point to a syn-deformational metamorphic event in which pyrite has been abraded (rounded), whereas pyrrhotite behavior was largely, although not necessarily entirely, ductile, and pentlandite underwent reincorporation into pyrrhotite and subsequent re-exsolution concentrated along the grain contacts with pyrite (Figure 5B). Pyrite displays the widest range of sizes and overprint textures (Figures 4 and 13–15). Among the key features of the pyrite are the foam textures and pinch-and-swell grain boundaries in the stringer sulfides outside the orebody that can be attributed to syn-deformational metamorphism and annealing (Figures 4E, 5D and 14).

Although Veloso et al. [20] acknowledged the importance of tectonic control on ore formation at Jatobá, direct evidence for deep burial metamorphism at amphibolite facies only came from the later identification of high-pressure ferrotschermakite inclusions in magnetite [54] and as discrete grains in the rock matrix. The origin and timing of initial sulfide formation are thus debatable, at least relative to that of the IOCG system, since the seafloor rift setting proposed [7,31] may have provided for a prior accumulation of sulfides (e.g., volcanic-hosted massive sulfide; VHMS), prior to any IOCG overprint.

The geochemical signatures in pyrite defined by As, Ni, and Co concentrations (Figure 11A–D) coupled with LA-ICP-MS element maps (Figures 13–15) lead us to infer there are at least two distinct generations of pyrite growth both outside and within the orebody. The first, characteristically observed as (partially resorbed?) grain cores and thus the earliest, is defined by high Co concentrations at variable but generally low Ni concentrations. The second generation of pyrite is clearly later and has wide-ranging concentrations of As, Ni, and Co and, on some maps at least, shows a patchy oscillatory zoning, albeit disrupted or obliterated altogether, as exemplified by the complex overprinting textures illustrated in Figures 4F, 13–15. The distinct geochemical trends displayed on the plots of As vs. Co/Ni in pyrite recorded by pyrite outside and within the orebody, ~100 m apart (Figure 11C,D), may also be evidence for a multistage origin. The observed assemblage is thus considered the product of the metamorphism and deformational reworking of an early sulfide assemblage and a superimposed fluid event that introduced additional metals and further modified the assemblage. Although partially overlapping, the two events were not necessarily spatially coupled, and their temporal relationships remain ill-constrained.

Pyrite contains measurable concentrations of both Pd and Pt, even if Pd is an order of magnitude higher (mean 7.4 ppm) in pyrite from outside the orebody (Figure 12). The flat LA-ICP-MS depth profiles suggest that PGE are dissolved in the sulfide, yet the positive correlation between Pd and Ni, Te, Bi (and Sb, Ag), and Pt with As may suggest nanoscale inclusions of Pd-Bi-Te and Pt-As phases as much as solid solution, even if no nanoinclusions could be identified on the time-resolved downhole profiles.

A remarkable and hitherto unrecognized PGM signature is seen in Jatobá pyrite (Figure 5D–M, Figures 6–8), largely restricted to fractures and pressure shadows in pyrite. The more diverse range of mineral species and greater size of individual PGM in orebody pyrite contrasts with a dominance of abundant yet smaller grains of merenskyite in pyrite from outside the orebody. In the latter case, ductile migration of chalcopyrite along pinch and swell textures is accompanied by PGM nucleation, suggesting formation in the waning stages of deformation from PGE released from the annealed pyrite (Figure 5D–I). In contrast, sustained fluid infiltration would result in PGM coarsening and deposition of abundant gangue minerals (e.g., biotite, apatite, quartz) like those observed along the PGM-trails or close to grain boundaries in orebody pyrite (Figure 5J–M). Any PGE that was contained in solid solution within the sulfide minerals was likely expelled and remobilized during metamorphism and shearing.

The relative differences in terms of Pd and Pt concentrations in pyrite and the size of the discrete PGM within and outside the orezone are likely explained by the more intense overprinting of the latter during tectonic activation of the shear zone hosting the orebody.

The better preservation of deformation textures in pyrite outside the orebody is attributable to the dry conditions operating during prograde metamorphism. The fluids associated with retrograde metamorphism were largely focused along crustal shear zones, generating IOCG-style mineralization, associated alteration, and more extensive reworking of ore textures. Under such conditions, an input of metals and sulfur from deeper basement can be hypothesized to account for the potassic-Fe metasomatism defining the onset of IOCG mineralization. This is consistent with the available isotopic evidence (e.g., [58]), indicating multiple but largely mantle- and magmatic-derived sulfur and the involvement of highly saline, hot, and deep-seated metalliferous fluids. The characteristic accessory mineral signature of IOCG deposits, notably the relative abundance of REE, U-, and W-bearing minerals (apatite, allanite, uraninite, huttonite or thorite, ferberite, and scheelite) is especially pronounced throughout the magnetite-rich orebody.

5.2. PGM in Ni-Bearing Sulfides—Identifying the Potential Source

A positive correlation exists between the PGE content of present-day seafloor massive sulfide (SMS) and PGE enrichment in their ancient VMS analogues. For example, active seafloor deposits of the PACMANUS hydrothermal field, eastern Manus basin, Papua New Guinea, contain 356 ppb Pd [59], remarkably similar to VMS ores from the Iberian Pyrite Belt (203–350 ppb ΣPGE; [60]. These PGE concentrations are within the range reported for Jatobá [53]. Such a SMS-like scenario might be invoked for the initial deposition of Ni- and PGE-bearing sulfides at Jatobá, considering the volcanic sequence hosting the deposit. The stringer sulfides outside the magnetite-rich intervals preserve the initial conditions better than the ores since they have been less affected by fluid infiltration along shear zones. We cannot, however, fully rule out a potential source of a different genetic type, provided that PGE are increasingly identified in 'non-traditional' deposits, including porphyry copper deposits (e.g., [61]).

Whatever the primary source of PGE, was the fluid that transported the PGE directly derived from magma, or alternatively, a product of seafloor hydrothermal alteration via convective cells leaching PGE from the host volcanics? Studies have shown that Cu-rich sulfides, like those at Jatobá, likely relate to a magmatic source, whereas Zn-rich SMS correspond to the second hypothesis (e.g., [59]). On the other hand, the PGE geochemistry of the volcanic rocks is considered to control the chalcophile element fertility of VMS mineralization, as was, for example, shown in the study of the Jaguar and Bentley VMS-style Cu–Zn deposits in Western Australia [62]. VHMS have long been suspected and indeed invoked by Melo et al. [41], but they have never been unambiguously confirmed in the Carajás Domain. They would certainly be expected in the Neoarchean Itacaiúnas Supergroup or in the older Rio Novo Group, as suggested by Costa et al. [31], perhaps also considering the presence of iron formations in the same sequences.

PGE have been used to test the hypothesis that the time of sulfide saturation, relative to volatile saturation, also controls the fertility of porphyry Cu and porphyry Cu–Au deposits [63], and references therein. Indeed, the enrichment of PGE in porphyry Cu-Au deposits is well documented in a variety of metallogenic belts (e.g., [64], and references therein). A relative enrichment in PGE is considered to occur during the high-T potassic alteration stage of porphyry deposit formation [64]. Although a comparable scenario could have been involved at Jatobá, no prospective magmatic source for a derived IOCG fluid, such as granite, has been identified. Porphyry-type mineralization has not been observed in the Carajás Domain, but this discourse serves to illustrate that PGE are not restricted to ore systems associated with mafic-ultramafic rocks as popularly yet falsely believed.

5.3. Which Ore Genesis Model Best Explains the Evidence?

Data in the present contribution show that Jatobá is not only a Ni-bearing sulfide deposit of probable IOCG-type hosted within a sequence dominated by mafic rocks, but also that it stands out from other Ni-bearing IOCG deposits in the Carajás Domain in terms of a relative enrichment of Pd and Pt, expressed as both measurable PGE in sulfides and as discrete PGM. Two alternative genetic models for the deposit are supported, at least in part, by observations of ore mineralogy, textures, and geochemical signatures of the main minerals and are compounded by the local geological and structural setting.

The favored model envisages two distinct stages of mineralization. Pre-existing stringer sulfides of as-yet poorly constrained origin within a mafic rock pile contain both Ni and PGE and are superposed by a strongly focused flow of metal-bearing fluids along crustal shears, resulting in IOCG-style mineralization with evidence of replacement and overprinting. The presence of Ni and PGE from pre-existing mineralization, combined with elements more typical of IOCG deposits, including REE and U, led to the observed assemblage, notably the diverse suite of platinum group minerals illustrated in Figures 5–8. Noting the abundance of Sb, Te, Se, and Bi in Ni-PGE deposits like Norilsk [65] as much as in IOCG deposits, these elements could be derived from either the pre-existing Ni-PGE source or from the IOCG fluids.

An alternative model considers IOCG-type fluids that have dissolved and remobilized Ni and PGE from pre-existing mineralization within the mafic sequence hosting the ores, from basement rocks at depth, or even from the host rocks themselves, and re-concentrated them along structural conduits. Potential sources would include komatiites and ultramafic rocks in the basement. Both are well documented in the region. Mesoarchean komatiites would be a major source for Ni (and subordinate PGE). We note descriptions of spinifex textures in proximity to Jatobá [28]. Unfortunately, due to extensive soil and forest cover in the area and the play of tectonics, it is impossible to ascertain with any certainty whether these komatiites belong to the Mesoarchean greenstone sequences, or to the Neoarchean Itacaiúnas Supergroup. If the former could be confirmed, it would also explain the evidence for pre-IOCG amphibolite facies metamorphism in the magnetite-sulfide assemblages reported by Campo-Rodriguez et al. [54]. Such a model would also be concordant with the occurrence of several other Ni-rich IOCG deposits nearby and their apparent concentration in the southern copper belt (Jaguar, GT-34, Cristalino, and Castanha), close to the Rio Maria TTG-greenstone domain.

Although the mobility of both Pt and Pd has been well documented in experimental studies (e.g., [66–68]) and many Ni-PGE ores display overprinting, either in the waning stages of formation or during later metamorphic-deformation events (e.g., [69]), there are relatively few antecedents for large-scale remobilization and re-concentration of PGE and related metals. Wang et al. [70] describe the redistribution and re-concentration of ore-forming metals in the Huangshandong deposit, China, while a second example comes from another part of Brazil [71], in which parts of the komatiite-hosted Fortaleza de Minas deposit are remobilized and subsequently redeposited as discordant veins. Hydrothermal nickel deposits (e.g., [21,72]) also appear proximal relative to the source and are often relatively small in scale).

Except for the Pt-arsenide sperrylite, the speciation of all PGM observed in the present study is conspicuous because Pd is combined only with highly mobile elements such as Te, Bi, and Sb, all of which are typically present in IOCG fluids. They are strongly associated with REE- and U-bearing minerals typical of IOCG mineralization, such as britholite and uraninite.

Metamorphism in the Carajás Domain has traditionally been considered as a single event at ~2.82 Ga that was restricted to the basement. Rocks of the Itacaíúnas Supergroup are not considered to display evidence of regional metamorphism. Nevertheless, a study by Fernandes et al. [73] of an area in western Carajás describes a ca. 2.7 Ga dynamic metamorphic event as having "reached amphibolite-facies conditions and overprinted previous metamorphic textures" in basement rocks. The same authors also describe "chalcopyrite-

rich amphibole and amphibole schist concordant with metamorphic foliation". These are considered amphibolites, representing the metamorphosed expression of mafic protoliths belonging to a volcano-sedimentary succession in the Sao Felix Group of the Itacaíúnas Supergroup. Other authors (e.g., [8]) favored a later "dynamic metamorphism", implying only very low temperatures and essentially inducing only mechanical changes, to account for the mylonitic fabrics observed in alteration assemblages in IOCG deposits of the Carajás Domain. The high-pressure conditions (ca. 6.4–7.4 kbar) estimated from the composition of ferrochermakite in magnetite [54]) represent a hitherto unrecognized "smoking gun" that cannot be easily ignored. Both they and the syn-deformational textures displayed by pyrite are, however, entirely compatible with amphibolite facies metamorphism. Formation of the ore textures and the relationships between minerals illustrated in the present contribution can only be attributed to deformation at conditions of burial, with applied heat and pressure approximating to amphibolite facies, clearly more than the near-surface brittle deformation episode invoked for "dynamic metamorphism" by other authors.

Both models remain conjectural without additional supporting evidence or geochronological constraints, and each has advantages and drawbacks, possibly indicating a more complex sequence of events that incorporates elements of both models. Evidence is needed to constrain the timing of copper precipitation, the nature and age of any pre-existing mineralization, or the relative timing of the IOCG overprinting event(s). Do they, for example, represent stages within a (semi)-continuous evolution (e.g., prograde and retrograde cycles within a single metamorphic event)? We cannot discount a hybrid model involving both dissolution-remobilization-reprecipitation from depth and in-situ replacement.

6. Conclusions and Implications

Jatobá is recognized as a structurally controlled IOCG deposit based on the main commodities, the abundance of iron oxides, and the observed styles of alteration. It is conspicuous in terms of the contained nickel and the remarkable co-enrichment of Pd and Pt. Observations of ore mineralogy, textures, and the geochemical signatures of the main minerals, compounded by the local geological and structural setting, allow a tentative genetic model to be proposed. Although speculative and not yet tied to specific geological events or validated by geochronological evidence, one scenario for Jatobá considers that both Ni and PGE were contained within pre-existing sulfides, possibly resulting from precipitation in a VHMS-like setting within a mafic rock pile, onto which the IOCG-style mineralization was superposed. The IOCG overprint is recorded by replacement and local-scale remobilization, in which PGE are largely though not completely, released from sulfides and combine with components of the IOCG fluids like Sb, Bi, and Te to form the range of PGM observed, notably tellurides and antimonides, as well as their association with REE- and U-bearing minerals typical of IOCG systems. An alternative model also involves fluids of hydrothermal or crustal origin but assumes a single influx of fluid instead of overprinting and partially replacing existing mineralization. In this case, the fluid dissolved and remobilized Ni and PGE from pre-existing mineralization located within (e.g., from komatiites) within the mafic sequence or from the basement (ultramafic rocks) and re-concentrated them within a pre-existing oxide assemblage, possibly during the retrograde stage of regional metamorphism at amphibolite facies.

LA-ICP-MS analysis of pyrite from Jatobá revealed concentrations of Pd and Pt well above the minimum limits of detection, with clear, flat signals indicative of incorporation within the crystal lattice. We were also able to identify an enrichment of both Pd and Pt within healed fractures in Jatobá pyrite on element maps. Most importantly, in terms of recognizing the PGE-enriched character of the Jatobá deposit, is the identification of more than half a dozen distinct PGMs. Although PGE mineralization is documented from the Carajás Domain in deposits such as Luanga associated with mafic-ultramafic intrusions [47] and enigmatic deposits like Serra Pelada [49], our new data thus represent the first description of discrete PGM and sulfide-hosted PGM within mineralization from a deposit considered an IOCG-type deposit. Further study of representative samples is

recommended to evaluate the deposit-scale distribution of PGM at Jatobá, the average grade of PGM and Ni, and the degree to which these grades correlate with Cu. If the PGE enrichment can be confirmed across the deposit, future work might also aim to adequately understand the geometallurgical implications of PGE enrichment in Jatobá ores.

The discovery of PGE at Jatobá emphasizes the potential for additional discoveries in structurally and lithologically comparable sulfide ore systems in which Ni enrichment is recognized. The PGM identified are small, largely restricted to filled fractures in pyrite, and thus will only be identified by analysis for PGE, high-magnification imaging, and using LA-ICP-MS to drill down with a large spot size and high Hz to look for elevated PGE counts. Specimens would also need to be carefully prepared and polished to avoid plucking out of phases from grain boundaries. Further examples of analogous mineralization outside the Carajás district that combine the characteristics of magmatic Ni-PGE and IOCG-style mineralization may be rare but are certainly not impossible, extending the diversity of deposit types that may be vital sources of PGE supply in the future.

Supplementary Materials: The following supporting information can be downloaded at: https://www.mdpi.com/article/10.3390/min14080757/s1, Table S1. (LA-ICP-MS trace element data for sulfide minerals (complete dataset, element concentrations in ppm).

Author Contributions: Y.T.C.R.: conceptualization, experimental, validation, writing—original draft. N.J.C.: conceptualization, writing—original draft, supervision. C.L.C.: writing—original draft, supervision. M.E.S.: conceptualization, supervision. S.A.K. and S.G.: experimental. K.E.: validation, guidance and discussion. All authors have read and agreed to the published version of the manuscript.

Funding: Y.T.C.R. and M.E.S. acknowledges continuous support from the Brazilian Research Council (CNPq—Project 409015/2021-0) and the Coordenação de Aperfeiçoamento de Pessoal de Nível Superior—Brasil (CAPES)—Finance Code 001. Analytical expenses were supported by a grant from the Institute of Sustainability, Energy and Resources, The University of Adelaide. N.J.C. and K.E. acknowledge funding through Australian Research Council Linkage grant LP200100156 (Critical Minerals from Complex Ores).

Data Availability Statement: Data will be made available on request.

Acknowledgments: We acknowledge the constructive comments from two anonymous reviewers that helped us improve expression and clarity.

Conflicts of Interest: The authors declare that they have no known competing financial interests relevant to the reported research.

References

1. Barton, M. Iron oxide (-Cu-Au-REE-P-Ag-U-Co) systems. In *Treatise on Geochemistry*, 2nd ed.; Elsevier: Amsterdam, The Netherlands, 2014; Volume 13, pp. 515–541.
2. Skirrow, R.G. Iron oxide copper-gold (IOCG) deposits-a review (part 1): Settings, mineralogy, ore geochemistry and classification. *Ore Geol. Rev.* **2022**, *140*, 104569. [CrossRef]
3. Hitzman, M.W.; Oreskes, N.; Einaudi, M.T. Geological characteristics and tectonic setting of Proterozoic iron oxide (Cu-U-Au-REE) deposits. *Precambr. Res.* **2002**, *58*, 241–287. [CrossRef]
4. Bidgood, A.; Hitzman, M. New models to aid the discovery of critical raw material deposits for the Green Stone Age. In *The Green Stone Age: Exploration and Exploitation of Minerals for Green Technologies*; Smelror, M., Hanghøj, K., Schiellerup, H., Eds.; Geological Society, London, Special Publications: London, UK, 2022; Volume 526, pp. 183–191. [CrossRef]
5. Grainger, C.J.; Groves, D.I.; Tallarico, F.H.B.; Fletcher, I.R. Metallogenesis of the Carajás mineral province, southern Amazon Craton, Brazil: Varying styles of Archean through Paleoproterozoic to Neoproterozoic base- and precious-metal mineralisation. *Ore Geol. Rev.* **2008**, *33*, 451–489. [CrossRef]
6. Monteiro, L.V.S.; Xavier, R.P.; de Souza Filho, C.R.; Moreto, C. Metalogênese da Província Carajás. In *Metalogênese das Províncias Tectônicas Brasileiras*; da Glória da Silva, M., da Costa Neto, M.B., Jost, H., Kuyumjian, R.M., Eds.; CPRM Serviço Geológico do Brasil: Belo Horizonte, Brazil, 2014; pp. 43–92.
7. Tavares, F.M.; Trouw, R.A.J.; Silva, C.M.G.; Justo, A.P.; Oliveira, J.K.M. The multistage tectonic evolution of the northeastern Carajás Province, Amazonian Craton, Brazil: Revealing complex structural patterns. *J. S. Am. Earth Sci.* **2018**, *88*, 238–252. [CrossRef]

8. Schutesky, M.E.; de Oliveira, C.G. From the roots to the roof: An integrated model for the Neoarchean Carajás IOCG System, Brazil. *Ore Geol. Rev.* **2020**, *127*, 103833. [CrossRef]
9. Trunfull, E.F.; Hagemann, S.G.; Xavier, R.P.; Moreto, C.P.N. Critical assessment of geochronological data from the Carajás Mineral Province, Brazil: Implications for metallogeny and tectonic evolution. *Ore Geol. Rev.* **2020**, *121*, 103556. [CrossRef]
10. Toledo, P.I.F.; Moreto, C.P.N.; Monteiro, L.V.S.; Melo, G.H.C.; Matos, F.M.V.; Xavier, R.P.; Carvalho, J.A.; Filho, C.A.M.; Navarro, M.S.; Lana, C.C. Breaking up the temporal link between granitic magmatism and iron oxide-copper-gold (IOCG) deposits in the Carajás Mineral Province, NW Brazil. *Miner. Depos.* **2024**, *59*, 601–625. [CrossRef]
11. Xavier, R.P.; Soares Monteiro, L.V.; Moreto, C.P.N.; Pestilho, A.L.S.; Coelho de Melo, G.H.; Delinardo da Silva, M.A.; Aires, B.; Ribeiro, C.; Freitas e Silva, F.H. The Iron Oxide Copper-Gold Systems of the Carajás Mineral Province, Brazil. In *Geology and Genesis of Major Copper Deposits and Districts of the World: A Tribute to Richard H. Sillitoe*; Hedenquist, J.W., Harris, M., Camus, F., Eds.; Society of Economic Geologists: Littleton, CO, USA, 2012; Volume 16, 22p.
12. Monteiro, L.V.S.; Xavier, R.P.; Carvalho, E.R.; Hitzman, M.W.; Johnson, C.A.; Souza, C.R.; Filho, C.R.; Torresi, I. Spatial and temporal zoning of hydrothermal alteration and mineralization in the Sossego iron oxide-copper-gold deposit Carajás Mineral Province, Brazil: Paragenesis and stable isotope constraints. *Miner. Depos.* **2008**, *43*, 129–159. [CrossRef]
13. Monteiro, L.V.; Xavier, R.P.; Hitzman, M.W.; Juliani, C.; de Souza Filho, C.R.; Carvalho, E.D. Mineral chemistry of ore and hydrothermal alteration at the Sossego iron oxide-copper-gold deposit, Carajás Mineral Province, Brazil. *Ore Geol. Rev.* **2008**, *34*, 317–336. [CrossRef]
14. Moreto, C.P.N.; Monteiro, L.V.S.; Xavier, R.P.; Creaser, R.A.; Dufrane, S.A.; Tassinari, C.C.G.; Sato, K.; Kemp, A.I.S.; Amaral, W.S. Neoarchean and Paleoproterozoic iron oxide-copper-gold events at the Sossego deposit, Carajás Province, Brazil, Re-Os and U-Pb geochronological evidence. *Econ. Geol.* **2015**, *110*, 809–835. [CrossRef]
15. Tassinari, C.C.G.; Mellito, M.K.; Babinski, M. Age and origin of the Cu (Au-Mo-Ag) Salobo 3A ore deposit, Carajás Mineral Province, Amazonian Craton, northern Brazil. *Episodes* **2003**, *26*, 2–9. [CrossRef]
16. Melo, G.H.C.; Monteiro, L.V.S.; Xavier, R.P.; Moreto, C.P.N.; Santiago, E.S.B.; Dufrane, S.A.; Aires, B.; Santos, A.F.F. Temporal evolution of the giant Salobo IOCG deposit, Carajás Province (Brazil): Constraints from paragenesis of hydrothermal alteration and U-Pb geochronology. *Miner. Depos.* **2017**, *52*, 709–732. [CrossRef]
17. Campo-Rodríguez, Y.T.; Schutesky, M.E.; de Oliveira, C.G.; Whitehouse, M.J. Unveiling the polyphasic evolution of the Neoarchean IOCG Salobo deposit, Carajás Mineral Province, Brazil: Insights from magnetite trace elements and sulfur isotopes. *Ore Geol. Rev.* **2021**, *140*, 104572. [CrossRef]
18. Tallarico, F.H.B.; Figueiredo, B.R.; Groves, D.I.; Kositcin, N.; McNaughton, N.J.; Fletcher, I.R.; Rego, J.L. Geology and SHRIMP U-Pb geochronology of the Igarape Bahia Deposit, Carajás copper-gold belt, Brazil, an Archean (2.57 Ga) example of iron-oxide Cu-Au-(U-REE) mineralization. *Econ. Geol.* **2005**, *100*, 7–28. [CrossRef]
19. de Melo, G.H.C.; Monteiro, L.V.S.; Xavier, R.P.; Moreto, C.P.N.; Santiago, E. Tracing Fluid Sources for the Salobo and Igarape Bahia Deposits: Implications for the Genesis of the Iron Oxide Copper-Gold Deposits in the Carajás Province, Brazil. *Econ. Geol.* **2019**, *114*, 697–718. [CrossRef]
20. Veloso, A.S.R.; Monteiro, L.V.S.; Juliani, C. The link between hydrothermal nickel mineralization and an iron oxide-copper-gold (IOCG) system: Constraints based on mineral chemistry in the Jatobá deposit, Carajás Province. *Ore Geol. Rev.* **2020**, *121*, 103555. [CrossRef]
21. González-Álvarez, I.; Pirajno, F.; Kerrich, R. Hydrothermal nickel deposits: Secular variation and diversity. *Ore Geol. Rev.* **2013**, *52*, 1–3. [CrossRef]
22. Oliveira, M.M.F. Caracterização e Metalogênese do Depósito de Ni do Jaguar, Província Mineral de Carajás. Master's Thesis, Universidade de Brasília, Brasília, Brazil, 2017; 115p.
23. Ferreira Filho, C.F.; Ferraz de Oliveira, M.M.; Mansur, E.T.; Rosa, W.D. The Jaguar hydrothermal nickel sulfide deposit: Evidence for a nickel-rich member of IOCG-type deposits in the Carajás Mineral Province, Brazil. *J. S. Am. Earth Sci.* **2021**, *111*, 103501. [CrossRef]
24. Mansur, E.T.; Dare, S.A.S.; Ferreira Filho, C.F.; Rodrigues Miranda, A.C.; Soares Monteiro, L.V. The distribution of trace elements in sulfides and magnetite from the Jaguar hydrothermal nickel deposit: Exploring the link with IOA and IOCG deposits within the Carajás Mineral Province, Brazil. *Ore Geol. Rev.* **2023**, *152*, 105256. [CrossRef]
25. Garcia, V.B.; Schutesky, M.E.; Oliveira, C.G.; Whitehouse, M.J.; Huhn, S.R.B.; Augustin, C.T. The Neoarchean GT-34 Ni deposit, Carajás mineral Province, Brazil: An atypical IOCG-related Ni sulfide mineralization. *Ore Geol. Rev.* **2020**, *127*, 103773. [CrossRef]
26. Craveiro, G.S.; Xavier, R.P.; Villas, R.N.N. The Cristalino IOCG deposit: An example of multi-stage events of hydrothermal alteration and copper mineralization. *Braz. J. Geol.* **2019**, *49*, e20180015. [CrossRef]
27. Pestilho, A.L.S.; Monteiro, L.V.S.; de Melo, G.H.C.; Moreto, C.P.N.; Juliani, C.; Fallick, A.E.; Xavier, R.P. Stable isotopes and fluid inclusion constraints on the fluid evolution in the Bacaba and Castanha iron oxide-copper-gold deposits, Carajás Mineral Province, Brazil. *Ore Geol. Rev.* **2020**, *126*, 103738. [CrossRef]
28. Siepierski, L.; Ferreira Filho, C.F. Spinifex-textured komatiites in the south border of the Carajás ridge, Selva Greenstone belt, Carajás Province, Brazil. *J. S. Am. Earth Sci.* **2016**, *66*, 41–55. [CrossRef]
29. Dutra, L.F.; Louro, V.H.A.; Monteiro, L.V.S. The southern IOCG and hydrothermal nickel mineralization trend of the Carajás Mineral Province: Airborne geophysical and remote sensing evidences for structural controls and hydrothermal signature. *J. Appl. Geophys.* **2023**, *213*, 105016. [CrossRef]

30. Vasquez, L.V.; Rosa-Costa, L.R.; Silva, C.G.; Ricci, P.F.; Barbosa, J.O.; Klein, E.L.; Lopes, E.S.; Macambira, E.B.; Chaves, C.L.; Carvalho, J.M.; et al. *Geologia e Recursos Minerais do Estado do Pará: Sistema de Informações Geográficas-SIG: Texto explicativo dos mapas Geológico e Tectônico e de Recursos Minerais do Estado do Pará 1:1.000.000*; CPRM: Belém, Brazil, 2008; 328p.
31. da Costa, F.G.; Araújo dos Santos, P.; de Oliveira Serafim, I.C.C.; Costa, I.S.L.; Roopnarain, S. From Mesoarchean drips to modern-style tectonics in the Carajás Province, Amazonian Craton. *J. S. Am. Earth Sci.* **2020**, *104*, 102817. [CrossRef]
32. Araújo, O.D.; Maia, R.G.N.; João, X.J.; Costa, J.B.S. A megaestruturação arqueana da folha Serra dos Carajás. In *Congresso Latino-Americano de Geologia*; SBG: Belém, Brazil, 1988; Volume 7, pp. 324–338.
33. Machado, N.; Lindenmayer, Z.; Krogh, T.E.; Lindenmayer, D. U-Pb geochronology of Archean magmatism and basement reactivation in the Carajás area, Amazon shield, Brazil. *Precambr. Res.* **1991**, *49*, 329–354. [CrossRef]
34. Martins, P.L.G.; Toledo, C.L.B.; Silva, A.M.; Chemale, F., Jr.; Santos, J.O.S.; Assis, L.M. Neoarchean magmatism in the southeastern Amazonian Craton, Brazil: Petrography, geochemistry and tectonic significance of basalts from the Carajás Basin. *Precambr. Res.* **2017**, *302*, 340–357. [CrossRef]
35. DOCEGEO. Revisão litoestratigráfica da província mineral de Carajás. In *Litoestratigrafia e Principais Depósitos Minerais, Proceedings of the Anexo do 35. Congresso Brasileiro de Geologia, Belém, Brazil, 1988*; SBG, Anexo aos anais: Belém, Brazil, 1988; Volume 35, pp. 11–54.
36. Feio, G.R.L.; Dall'Agnol, R.; Dantas, E.L.; Macambira, M.J.B.; Santos, J.O.S.; Althoff, F.J.; Soares, J.E.B. Archean granitoid magmatism in the Canaã dos Carajás area: Implications for crustal evolution of the Carajás province, Amazonian Craton, Brazil. *Precambr. Res.* **2013**, *227*, 157–185. [CrossRef]
37. Moreto, C.P.N.; Monteiro, L.V.S.; Xavier, R.P.; Creaser, R.A.; Dufrane, S.A.; Melo, G.H.C.; Silva, M.A.D.; Tassinari, C.C.G.; Sato, K. Timing of multiple hydrothermal events in the iron oxide-copper gold deposits of the Southern Copper Belt, Carajás Province, Brazil. *Miner. Depos.* **2015**, *50*, 517–546. [CrossRef]
38. Teixeira, M.F.B.; Dall'Agnol, R.; Santos, J.O.S.; de Oliveira, D.C.; Lamarão, C.N.; McNaughton, N.J. Crystallization ages of Paleoproterozoic A-type granites of Carajás province, Amazon craton: Constraints from U-Pb geochronology of zircon and titanite. *J. S. Am. Earth Sci.* **2018**, *88*, 312–331. [CrossRef]
39. Teixeira, W.; Hamilton, M.A.; Girardi, V.A.V.; Faleiros, F.M. U-Pb baddeleyite ages of key dyke swarms in the Amazonian Craton (Carajás/Rio Maria and Rio Apa areas): Tectonic implications for events at 1880, 1110 Ma, 535 Ma and 200 Ma. *Precambr. Res.* **2019**, *329*, 138–155. [CrossRef]
40. Araújo Filho, R.C.; Nogueira, A.C.R.; Araújo, R.N. New stratigraphic proposal of a Paleoproterozoic siliciclastic succession: Implications for the evolution of the Carajás Basin, Amazonian Craton, Brazil. *J. S. Am. Earth Sci.* **2020**, *102*, 102665. [CrossRef]
41. de Melo, G.H.C.; Monteiro, L.V.S.; Hunger, R.B.; Toledo, P.I.F.; Xavier, R.P.; Zhao, X.F.; Su, Z.K.; Moreto, C.P.N.; Pereira de Jesus, S.d.S.G. Magmatic-hydrothermal fluids leaching older seafloor exhalative rocks to form the IOCG deposits of the Carajás Province, Brazil: Evidence from boron isotopes. *Precambr. Res.* **2021**, *365*, 106412. [CrossRef]
42. Almeida, F.F.M.; Hasui, Y.; Brito Neves, B.B.; Fuck, R.A. Brazilian structural provinces: An introduction. *Earth Sci. Rev.* **1981**, *17*, 1–29. [CrossRef]
43. Xavier, R.P.; Moreto, C.; de Melo, G.H.C.; Toledo, P.; Hunger, R.; Delinardo, M.; Faustinoni, J.; Lopes, A.; Monteiro, L.V.S.; Previato, M.; et al. Geology and Metallogeny of Neoarchean and Paleoproterozoic Copper Systems of the Carajás Domain, Amazonian Craton, Brazil. In Proceedings of the Mineral Resources to Discover-14th SGA Biennial Meeting, Quebec, QC, Canada, 20–23 August 2017; pp. 899–902.
44. Teixeira, A.S.; Ferreira Filho, C.F.; Della Giustina Schutesky, M.E.; Araújo, S.M.; da Silva, H.H.A.B. Geology, petrology and geochronology of the Lago Grande layered complex: Evidence for a PGE-mineralized magmatic suite in the Carajás Mineral Province, Brazil. *J. S. Am. Earth Sci.* **2015**, *64*, 116–138. [CrossRef]
45. Diella, V.; Ferrario, A.; Girardi, V.A.V. PGE and PGM in the Luanga mafic-ultramafic intrusion in Serra dos Carajás (Pará State, Brazil). *Ore Geol. Rev.* **1995**, *9*, 445–453. [CrossRef]
46. Mansur, E.T.; Ferreira Filho, C.F. Magmatic structure and geochemistry of the Luanga Mafic-Ultramafic Complex: Further constraints for the PGE-mineralized magmatism in Carajás, Brazil. *Lithos* **2016**, *266–267*, 28–43. [CrossRef]
47. Mansur, E.T.; Ferreira Filho, C.F.; Oliveira, D.P.L. The Luanga deposit, Carajás Mineral Province, Brazil: Different styles of PGE mineralization hosted in a medium-size layered intrusion. *Ore Geol. Rev.* **2020**, *118*, 103340. [CrossRef]
48. Moroni, M.; Girardi, V.A.; Ferrario, A. The Serra Pelada Au-PGE deposit, Serra dos Carajás (Pará State, Brazil): Geological and geochemical indications for a composite mineralising process. *Miner. Depos.* **2001**, *36*, 768–785. [CrossRef]
49. Cabral, A.R.; Lehmann, B.; Kwitko, R.; Costa, C.H.C. The Serra Pelada Au-Pd-Pt deposit, Carajás mineral province, northern Brazil: Reconnaissance mineralogy and chemistry of very high grade palladian gold mineralization. *Econ. Geol.* **2002**, *97*, 1127–1138. [CrossRef]
50. Cabral, A.R.; Lehmann, B.; Burgess, R. Late Cretaceous bonanza-style metal enrichment in the Serra Pelada Au-Pd-Pt deposit Pará Brazil. *Econ. Geol.* **2011**, *106*, 119–125. [CrossRef]
51. Pollard, P.J.; Taylor, R.G.; Peters, L.; Matos, F.; Freitas, C.; Saboia, L.; Huhn, S. 40Ar-39Ar dating of Archean iron oxide Cu-Au and Paleoproterozoic granite-related Cu-Au deposits in the Carajás Mineral Province, Brazil: Implications for genetic models. *Miner. Depos.* **2018**, *54*, 329–346. [CrossRef]

52. Lancaster, J.O.; Fanton, J.; Almeida, A.J.; Leveille, R.A.; Vieira, S. Discovery and geology of the Sossego copper-gold deposit, Carajás District, Pará State, Brazil. In Proceedings of the 31st International Geological Congress, Rio de Janeiro, Brazil, 6–17 August 2000.
53. Veloso, A.S.R. Evolução Metalogenetica do Deposito de Cu-(Zn) Jatobá, Provincia Mineral de Carajás. Ph.D. Thesis, University of São Paolo, São Paulo, Brazil, 2017; 197p.
54. Campo-Rodriguez, Y.T.; Ciobanu, C.L.; Slattery, A.; Cook, N.J.; Schutesky, M.E.; Ehrig, K.; King, S.A.; Yao, J. Polysomatic intergrowths between amphiboles and non-classical pyriboles in magnetite: Smallest-scale features recording a protracted geological history. *Am. Mineral.* 2024, *in press*. [CrossRef]
55. Belousov, I.; Danyushevsky, L.; Goemann, K.; Gilbert, S.; Olin, P.; Thompson, J.; Lounejeva, E.; Garbe-Schönberg, D. STDGL3, a reference material for analysis of sulfide minerals by Laser Ablation ICP-MS: An assessment of matrix effects and the impact of laser wavelengths and pulse widths. *Geostand. Geoanal. Res.* **2023**, *47*, 493–508. [CrossRef]
56. Gilbert, S.; Danyushevsky, L.; Robinson, P.; Wohlgemuth-Ueberwasser, C.; Pearson, N.; Savard, D.; Norman, M.; Hanley, J. A comparative study of five reference materials and the Lombard meteorite for the determination of the platinum-group elements and gold by LA-ICP-MS. *Geostand. Geoanalytical Res.* **2013**, *37*, 51–64. [CrossRef]
57. Paton, C.; Hellstrom, J.; Paul, B.; Woodhead, J.; Hergt, J. Iolite: Freeware for the visualisation and processing of mass spectrometric data. *J. Anal. At. Spectrom.* **2011**, *26*, 2508–2518. [CrossRef]
58. Santiago, E.S.B.; Xavier, R.P.; Hagemann, S.G.; Monteiro, L.V.S.; Cliff, J. Multiple sulfur isotopes constraints on origin and evolution of the Neoarchean and Paleoproterozoic Cu-Au systems from the Carajás Domain, Amazonian Craton, Brazil. *Ore Geol. Rev.* **2021**, *129*, 103872. [CrossRef]
59. Pašava, J.; Vymazalová, A.; Petersen, S.; Herzig, P. PGE distribution in massive sulfides from the PACMANUS hydrothermal field, eastern Manus basin, Papua New Guinea: Implications for PGE enrichment in some ancient volcanogenic massive sulfide deposits. *Miner. Depos.* **2004**, *39*, 784–792. [CrossRef]
60. Pašava, J.; Vymazalová, A.; Tornos, F. PGE distribution in massive sulfide deposits of the Iberian Pyrite Belt. *Miner. Depos.* **2007**, *42*, 309–314. [CrossRef]
61. McFall, K.; McDonald, I.; Wilkinson, J.J. Chapter 15: Assessing the role of tectono-magmatic setting in the precious metal (Au, Ag, PGE) and critical metal (Te, Se, Bi) endowment of porphyry Cu deposits. In *Tectonomagmatic Influences on Metallogeny and Hydrothermal Ore Deposits: A Tribute to Jeremy P. Richards (Volume II)*; Society of Economic Geologists: Littleton, CO, USA, 2021; Volume 2, pp. 277–295. [CrossRef]
62. Park, J.-W.; Campbell, I. Platinum-group element geochemistry of the volcanic rocks associated with the Jaguar and Bentley Cu-Zn volcanogenic massive sulfide (VMS) deposits, Western Australia: Implications for the role of chalcophile element fertility on VMS mineralization. *Miner. Depos.* **2021**, *56*, 583–600. [CrossRef]
63. Lowczak, J.N.; Campbell, I.H.; Cocker, H.; Park, J.W.; Cooke, D.R. Platinum-group element geochemistry of the Forest reef Volcanics, southeastern Australia: Implications for porphyry au-cu mineralisation. *Geochim. Cosmochim. Acta* **2018**, *220*, 385–406. [CrossRef]
64. Crespo, J.; Reich, M.; Barra, F.; Verdugo, J.J.; Martínez, C. Critical Metal Particles in Copper Sulfides from the Supergiant Río Blanco Porphyry Cu-Mo Deposit, Chile. *Minerals* **2018**, *8*, 519. [CrossRef]
65. Duran, C.J.; Barnes, S.J.; Pleše, P.; Prašek, M.K.; Zientek, M.L.; Pagé, P. Fractional crystallization-induced variations in sulfides from the Noril'sk-Talnakh mining district (polar Siberia, Russia). *Ore Geol Rev.* **2017**, *90*, 326–351. [CrossRef]
66. Barnes, S.J.; Liu, W. Pt and Pd mobility in hydrothermal fluids: Evidence from komatiites and from thermodynamic modelling. *Ore Geol. Rev.* **2012**, *44*, 49–58. [CrossRef]
67. Sullivan, N.A.; Zajacz, Z.; Brenan, J.M.; Tsay, A. The solubility of platinum in magmatic brines: Insights into the mobility of PGE in ore-forming environments. *Geochim. Cosmochim. Acta* **2022**, *316*, 253–272. [CrossRef]
68. Sullivan, N.A.; Zajacz, Z.; Brenan, J.M.; Hinde, J.C.; Tsay, A.; Yin, Y. The solubility of gold and palladium in magmatic brines: Implications for PGE enrichment in mafic-ultramafic and porphyry environments. *Geochim. Cosmochim. Acta* **2022**, *316*, 230–252. [CrossRef]
69. Mukwakwami, J.; Lafrance, B.; Lesher, C.M.; Tinkham, D.K.; Rayner, N.M.; Ames, D.E. Deformation, metamorphism, and mobilization of Ni-Cu-PGE sulfide ores at Garson Mine, Sudbury. *Miner. Depos.* **2014**, *49*, 175–198. [CrossRef]
70. Wang, S.M.; Wu, C.Z.; Muhtar, M.N.; Lei, R.X.; Brzozowski, M.J. Mobilization of ore-forming metals during post-magmatic hydrothermal overprinting of the Huangshandong Ni-Cu sulfide deposit, Eastern Tianshan, NW China. *Ore Geol. Rev.* **2021**, *137*, 104315. [CrossRef]
71. Almeida, C.M.; Olivo, G.R.; Carvalho, S.G. The Ni-Cu-PGE sulfide ores of the komatiite-hosted Fortaleza de Minas deposit, Brazil: Evidence of hydrothermal remobilization. *Can. Mineral.* **2007**, *45*, 751–773. [CrossRef]

72. Keays, R.R.; Jowitt, S.M. The Avebury Ni deposit, Tasmania: A case study of an unconventional nickel deposit. *Ore Geol. Rev.* **2013**, *52*, 4–17. [CrossRef]
73. Fernandes, C.M.D.; Galarza, M.A.; Teixeira de Gouvêa, R.C.; Tavares de Souza, H.P. Geochemical, geochronological, and isotopic constraints for the Archean metamorphic rocks of the westernmost part of the Carajás Mineral Province, Amazonian Craton, Brazil. *J. S. Am. Earth Sci.* **2021**, *110*, 103340. [CrossRef]